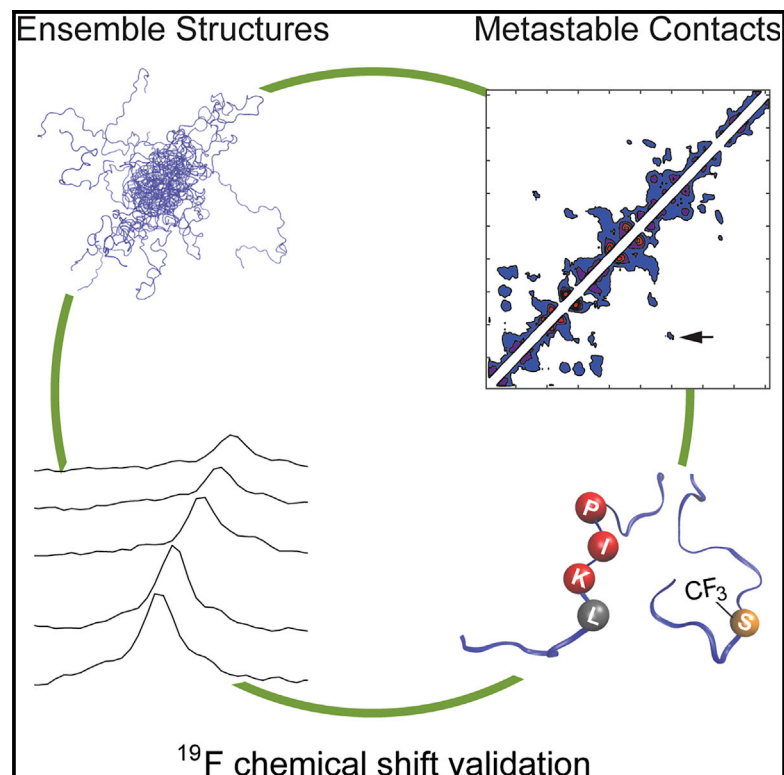# A Metastable Contact and Structural Disorder in the Estrogen Receptor Transactivation Domain

Graphical Abstract

Authors
Yi Peng, Shufen Cao, Janna Kiselar, ..., Witold K. Surewicz, Matthias Buck, Sichun Yang

Correspondence
sichun.yang@case.edu

In Brief
We unraveled that the transactivation domain of estrogen receptor is structurally disordered, yet unexpectedly compact, and that a metastable Ile33-Ser118 contact is observed to inhibit coactivator binding. Disruption by mutagenesis alters ensemble-structures and coactivator binding, providing a functional link of oncogenic Ser118 phosphorylation in breast cancer endocrine resistance.

Highlights

- A compact disorder is observed for the transactivation domain of estrogen receptor

- Multi-technique data integration determines ensemble-structures of protein disorder

- Contact map uncovers metastable, long-range contacts between Ile33 and Ser118

- ^{19}F NMR validates the role of contact metastability in receptor function

Article

A Metastable Contact and Structural Disorder in the Estrogen Receptor Transactivation Domain

Yi Peng,[1,8] Shufen Cao,[2,8] Janna Kiselar,[1] Xiangzhu Xiao,[2] Zhanwen Du,[1] An Hsieh,[1] Soobin Ko,[1] Yinghua Chen,[2] Prashansa Agrawal,[3] Wenwei Zheng,[4] Wuxian Shi,[1] Wei Jiang,[5] Lin Yang,[6] Mark R. Chance,[1,7] Witold K. Surewicz,[2] Matthias Buck,[2,7] and Sichun Yang[1,2,7,9,*]

[1]Center for Proteomics and Department of Nutrition, School of Medicine, Case Western Reserve University, Cleveland, OH 44106, USA
[2]Department of Physiology and Biophysics, School of Medicine, Case Western Reserve University, Cleveland, OH 44106, USA
[3]Chemistry-NMR Facility, Case Western Reserve University, Cleveland, OH 44106, USA
[4]College of Integrative Sciences and Arts, Arizona State University, Mesa, AZ 85212, USA
[5]Argonne Leadership Computing Facility, Argonne National Laboratory, Lemont, IL 60439, USA
[6]Photon Sciences Directorate, Brookhaven National Laboratory, Upton, NY 11973, USA
[7]Case Comprehensive Cancer Center, Case Western Reserve University, Cleveland, OH 44106, USA
[8]These authors contributed equally
[9]Lead Contact
*Correspondence: sichun.yang@case.edu
https://doi.org/10.1016/j.str.2018.10.026

SUMMARY

The N-terminal transactivation domain (NTD) of estrogen receptor alpha, a well-known member of the family of intrinsically disordered proteins, mediates the receptor's transactivation function. However, an accurate molecular dissection of NTD's structure-function relationships remains elusive. Here, we show that the NTD adopts a mostly disordered, unexpectedly compact conformation that undergoes structural expansion on chemical denaturation. By combining small-angle X-ray scattering, hydroxyl radical protein footprinting, and computational modeling, we derive the ensemble-structures of the NTD and determine its ensemble-contact map revealing metastable long-range contacts, e.g., between residues I33 and S118. We show that mutation at S118, a known phosphorylation site, promotes conformational changes and increases coactivator binding. We further demonstrate via fluorine-19 (^{19}F) nuclear magnetic resonance that mutations near I33 alter ^{19}F chemical shifts at S118, confirming the proposed I33-S118 contact in the ensemble of structural disorder. These findings extend our understanding of how specific contact metastability mediates critical functions of disordered proteins.

INTRODUCTION

The N-terminal transactivation domain (NTD) of estrogen receptor alpha is critical for the receptor's constitutive activation via its engagement with coactivator proteins to regulate transcriptional initiation (Lavery and McEwan, 2005; Metivier et al., 2000; Rajbhandari et al., 2012; Sadovsky et al., 1995; Tora et al., 1989; Warnmark et al., 2001). The NTD is an intrinsically disordered protein (IDP), a widely observed structural feature for trans-

activation domains in various members of the nuclear receptor superfamily (Kumar et al., 2013; Kumar and Thompson, 2012; Li et al., 2012) as well as many other transcription factors such as p53 (Dawson et al., 2003; Lee et al., 2010). Due to the functional significance of the NTDs, they are of interest for drug targeting. In particular, drug candidates that bind an intrinsically disordered region in the NTD of the androgen receptor (AR) have been developed (De Mol et al., 2016, 2018; Myung et al., 2013); however, understanding a drug's mechanism of action or the rationale of targeting the NTD usually requires in-depth insights into their molecular features. Such knowledge has been hindered by the difficulties in characterizing the structural ensembles of NTDs in particular and IDPs in general. In this paper, we specifically attempt to understand the structure-function relationships of the NTD of the estrogen receptor alpha (ERα) with regard to the structural features that determine its transactivation function.

Current knowledge about the ERα-NTD is limited due to the technical challenges of characterizing IDPs in general (Oldfield and Dunker, 2014; van der Lee et al., 2014). Only limited structural information is available for ERα-NTD from circular dichroism (CD) spectra and chemical shifts from nuclear magnetic resonance (NMR) spectroscopy (Rajbhandari et al., 2012; Warnmark et al., 2001). These have demonstrated that the isolated NTD is largely unstructured with poorly resolved chemical shifts, and with a high content of random coils and minimal helicity. Recently, biophysical techniques such as small-angle X-ray scattering (SAXS), fluorescence resonance energy transfer (FRET), and hydrogen exchange mass spectrometry (HX-MS) have revealed interesting structural features of IDPs (Berlow et al., 2017; Choy and Forman-Kay, 2001; Lindorff-Larsen et al., 2004; Russel et al., 2012), in particular RXRα-NTD (Belorusova et al., 2016), AR-NTD (Tien and Sadar, 2018), and PR-NTD (Kumar et al., 2013). The application of such approaches to ERα-NTD, however, has not been reported to date.

To investigate ERα-NTD structural features under native and denaturing conditions, we conducted multiple, in-solution biophysical studies using a recombinant ERα-NTD protein. We first acquired data from SAXS and HX-MS measurements for the native NTD. HX-MS confirms its overall structural disorder,
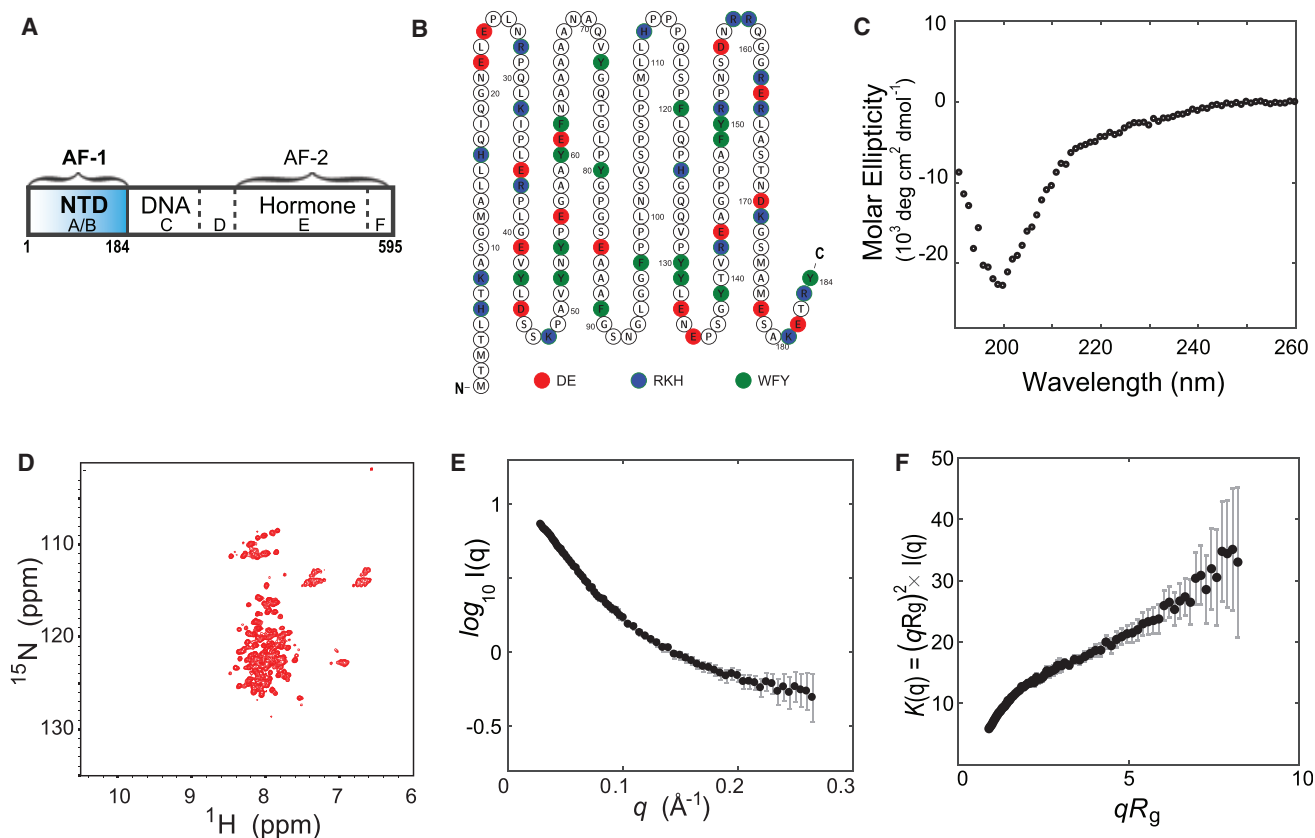
Figure 1. Structural Disorder of ERα-NTD
(A) Sub-domains of the ERα. Five domains are the NTD (A/B), a DNA-binding domain (C), a hinge region (D), a ligand-binding domain (E), and a short C-terminal domain (F).
(B) The 187-residue sequence. Charged and aromatic residues are highlighted in color.
(C) CD spectra for the NTD.
(D) Two-dimensional ^{1}H-^{15}N TROSY spectrum.
(E and F) Measured SAXS data yield the R_g value of 31.0 ± 0.2 Å and its dimensionless Kratky plot shows a structurally disordered characteristic.

consistent with the observation by CD and NMR, whereas SAXS data demonstrate that the NTD is more compact than expected. To examine the influence of chemical denaturants on the NTD, we acquired additional SAXS, CD, and ^{1}H-^{15}N NMR data for chemically denatured states and showed that the NTD undergoes structural expansion upon chemical denaturation, indicating a denaturant-dependent loss of structural features that drive the native compactness. To gain insights into the structural basis of this compact disorder, we performed all-atom explicit-solvent simulations to create a structural library of NTD conformations, and supplemented SAXS data with hydroxyl radical footprinting coupled with MS, which reports solvent accessibility for residue side chains (Huang et al., 2015; Takamoto and Chance, 2006; Wang and Chance, 2017). By combining these complementary techniques (Huang et al., 2018), we refine and assess ERα-NTD ensemble-structure models. Through the multi-technique data integration and contact map analyses, we identified long-range interactions involving residues S118 and I33 driving compactness within the ensemble and showed that S118 mutation mediates conformational changes and alters coactivator binding. Furthermore, through the means of fluorine-19 (^{19}F) NMR (Chrisman et al., 2018; Didenko et al., 2013; Kitevski-

LeBlanc and Prosser, 2012; Li et al., 2010; Matei and Gronenborn, 2016), we show that mutations near residue I33 alter ^{19}F chemical shifts at the position of residue S118, thereby confirming the proposed metastable I33-S118 contact in the ensemble. Overall, our multi-technique biophysical approach allowed us to elucidate specific structural features of the ERα-NTD that mediate its trans-activation function, and our findings raise important questions as to the potential of "contact metastability" to mediate functions for other nuclear receptors and/or IDPs in general.

RESULTS

Compact Disorder of ERα-NTD

We purified the ERα-NTD segment (SNA-M1-Y184; Figures 1A and 1B) via a refolding process from inclusion bodies of bacterial expression and conducted multiple biophysical measurements to confirm the structural disorder and structural features of this construct under native conditions. First, analysis of CD and 2D NMR spectra reaffirms the disordered nature of the native state as observed by Warnmark et al. (2001). Negative ellipticity at 200 nm indicates that the NTD has a high content of random coils with minimal helicity (Figure 1C). Moreover, the ^{1}H-^{15}N
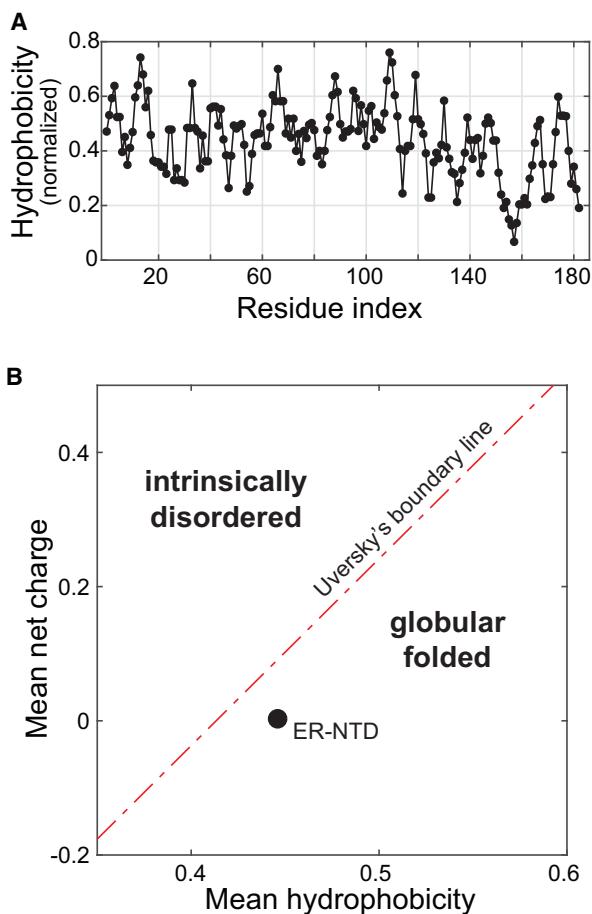
A

B

Figure 2. Biophysical Properties of Amino Acids in the NTD Sequence

(A) The hydrophobicity of NTD amino acids. Each was calculated by the Kyte-Doolittle approximation using the ExPASy server (with a window size of five amino acids). The hydrophobicity of individual residues was normalized to a scale of 0–1. The mean hydrophobicity $<H>$ is defined as the sum of the normalized hydrophobicities of all residues divided by the number of residues in the polypeptide, yielding a $<H>$ value at 0.446.

(B) The two-dimensional space of mean hydrophobicity $<H>$ and mean net charge $<q>$ of globular and intrinsically disordered proteins. The ERα-NTD is close to the Uversky's boundary line of $<H> = (<q> + 1.151)/2.785$, and enters the globular-fold regime.

transverse relaxation optimized spectroscopy (TROSY) data exhibit a characteristic spectral crowding in a random-coil region around the 8.0 ppm (Figure 1D) due to the NTD's limited chemical shift dispersion (Sahu et al., 2014). We confirm the overall lack of ordered secondary structure by HX-MS measurements (Bai et al., 1993; Buck et al., 1994; Craig et al., 2011; Englander and Kallenbach, 1983; Smirnovas et al., 2011). The HX-MS experiments show nearly 100% deuterium incorporation for the native NTD already after 1 min of exchange (Figure S1). The only region showing less than complete exchange maps to N- and C-terminal peptides 3–12 and 166–175, respectively. Even though this local protection is very small and potentially within the margin of a systematic or experimental error of the HX-MS measurements, it could also be explained by the presence of a small fraction of residual secondary structure under

native conditions as indicated by CD data (see below). Overall, these HX-MS data across the protein sequence suggest that this NTD construct is highly dynamic, consistent with a high level of structural disorder and very little ordered secondary structure as observed by 2D NMR and CD spectroscopy.

We next acquired SAXS data for the NTD in aqueous solution. This SAXS dataset together with related experimental details has been deposited into the Small-Angle Scattering Biological Databank (Valentini et al., 2015), with an SASBDB access code SASDEE2 (see also Table S1). The scattering intensity $I(q)$ (Figure 1E) yields a radius of gyration value of $R_g^{expt} = 31.0 \pm 0.2$ Å, using the Sosnick approach (Riback et al., 2017), which is in good consistency with the R_g values determined using other fitting methods (Table S2). A Kratky plot of $K(q) = (qR_g)^2 \times I(q)$ shows the characteristics of disordered or unfolded proteins (Figure 1F), compared with the bell-shaped $K(q)$ distribution typically observed in globular well-folded proteins. It is worth noting that many other IDPs approximately followed a power law of $R_g^{pred} = 2.54 \times N^{0.522}$ (Bernado and Svergun, 2012); using this power law, the predicted value is $R_g^{pred} = 39.0$ Å for the 187-residue NTD, considerably greater than the measured value, even when we consider experimental uncertainties. The apparent difference between R_g^{pred} and R_g^{expt} indicates that ERα-NTD adopts a more compact conformation in its naturally disordered state than would be generally expected for IDPs.

To further characterize the protein's biophysical properties, we calculated the mean hydrophobicity of the NTD at $<H> = 0.446$ (Figure 2A) using the normalized Kyte-Doolittle scale (Kyte and Doolittle, 1982; Wilkins et al., 1999), and determine its mean net charge $<q> = 0.003$ per residue based on the sequence (Figure 1B). Figure 2B shows that ERα-NTD deviates from the expected combination of $<H>$ and $<q>$ for IDPs in the two-dimensional H/q space, as it is seen to be to the "right" of Uversky's proposed boundary line that separates most IDPs and globular folds (Mao et al., 2010; Uversky, 2002). Of note, similar biophysical characteristics are observed for the 130-residue disordered RXRα-NTD, which has values of $<H> = 0.466$ and $<q> = 0.006$ (Belorusova et al., 2016), with placement at a similar location in the two-dimensional H/q space. Moreover, we find a balanced charge distribution for ERα-NTD at $f_+ = 0.080$ and $f_- = 0.086$, the fraction of negatively charged (Asp + Glu) and positively charged (Arg + Lys) residues, respectively, consistent with the "weak polyampholyte" regime of IDPs (Das and Pappu, 2013). Overall, these biophysical characteristics of ERα-NTD, at the boundary of native globular and disordered proteins, are consistent with the compact-disordered conformation that the NTD adopts.

Structural Expansion by Chemical Denaturation

To examine the effect of chemical denaturants on the NTD, we acquired CD data for the NTD in the presence of guanidine hydrochloride (GdnHCl), a chemical denaturant that can disrupt interactions driving the compactness. The minimal ellipticity at 222 nm observed for the native protein is reduced in the presence of GdnHCl (Figure 3A), indicating the existence of residual secondary structure in the native state. The ^1H-^{15}N TROSY NMR spectra also show increases in structural disorder upon addition of chemical denaturants (Figure 3B). In the latter experiment, GdnHCl was replaced by urea, a denaturing agent that is more compatible with NMR experiments. By overlapping the TROSY
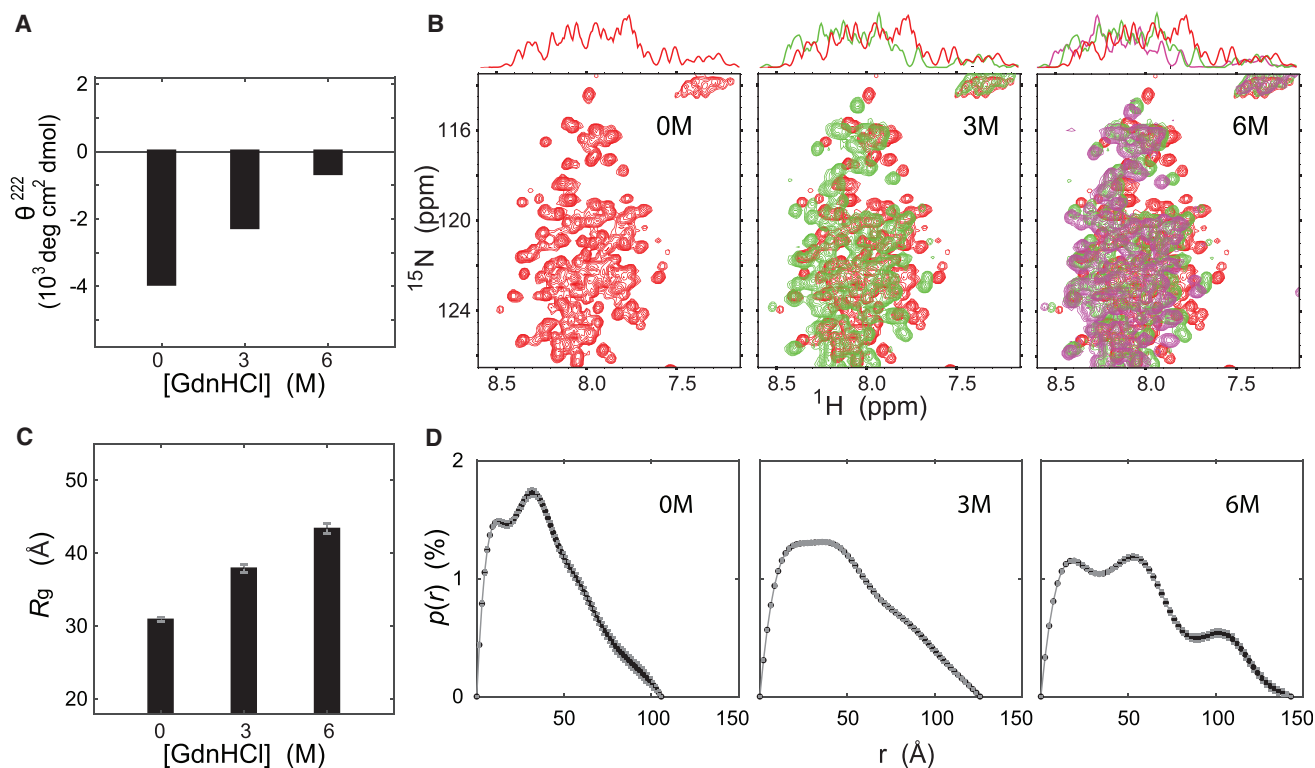
Figure 3. Structural Expansion by Chemical Denaturation

(A) CD signal at 222 nm for ERα-NTD in the presence of 0 M, 3 M, and 6 M GdnHCl, respectively.

(B) Two-dimensional ^{1}H-^{15}N TROSY spectra for the NTD in 0 M (red), 3 M (green), and 6 M (magenta) urea, respectively. On the top is the one-dimensional projection.

(C) SAXS-derived R_g values of 31.0 ± 0.2 Å, 38.0 ± 0.5 Å, and 43.4 ± 0.7 Å, respectively, using the Sosnick method (Riback et al., 2017).

(D) The pairwise distance distribution p(r) derived from experimental SAXS data. Calculated using AutoGnom (Svergun, 1992).

spectra for the NTD in the urea buffer, we observe that NMR peaks are gradually shifted to the downfield region and that the proton's chemical shift dispersion is narrowed (Figure 3B top). These NMR peak changes in the presence of a denaturant, together with reduced CD signal at 222 nm, indicate an increase in the level of structural disorder as well as a disappearance of residual secondary structure. We next acquired SAXS data for the NTD in the presence of 3 M and 6 M GdnHCl. Compared with the native R_g^{expt} value of 31.0 Å, the protein exhibits R_g^{expt} values of 38.0 Å and 43.4 Å in the presence of 3 M and 6 M GdnHCl, respectively (Figure 3C). The latter R_g^{expt} value for the denatured NTD is consistent with those reported for chemically denatured proteins via a power law (Kohn et al., 2004), by which we estimate a R_g^{pred} value of 44.0 Å for the denatured NTD. This denaturant-dependent size change for the NTD is also consistent with other IDP polypeptide chains that expand with increasing denaturant concentration (Borgia et al., 2016). In this case, however, the native NTD protein is more compact than expected for a typical IDP, and the structural changes seen in NMR and CD upon denaturation apparently disrupt interactions driving the compact state.

To further characterize this variation of the NTD conformation, we used SAXS data to estimate the pairwise distance distribution p(r), a histogram of all pairwise distances (r) between protein atoms. By using an indirect Fourier transformation (Svergun,

1992), we calculated the p(r) function. For native NTD, this function shows an asymmetric peak below r = 50 Å (Figure 3D), whereas in the presence of 3 M GdnHCl, it is considerably broadened (with a flat plateau), and more so in the presence of 6 M GdnHCl, in which it shows a broad distribution with a long tail up to r = 150 Å. The p(r) analysis shows that the NTD undergoes a considerable expansion from its native compactness with a large-scale stretching out of its polypeptide chain as a result of chemical denaturation.

Ensemble-Structures Constructed by Combining SAXS and FP-PF Data

As our studies reveal distinctive features for the native NTD, we attempt to determine the structural basis for the unexpectedly compact state. Given the low-resolution nature of SAXS, however, it is recognized that SAXS data alone are not sufficient to provide details of ensemble-structures. To gain additional information, sequence- or position-specific data from other techniques such as NMR and FRET have been used in conjunction with SAXS for characterizing IDPs (Borgia et al., 2016; Fuertes et al., 2017; Ganguly and Chen, 2009; Krzeminski et al., 2013; Zheng et al., 2016). Here, we supplement SAXS data by hydroxyl radical protein footprinting (FP) coupled with MS, where transforming the data to protection factors (PFs) can report solvent accessibility of residue side chains. The value of this approach
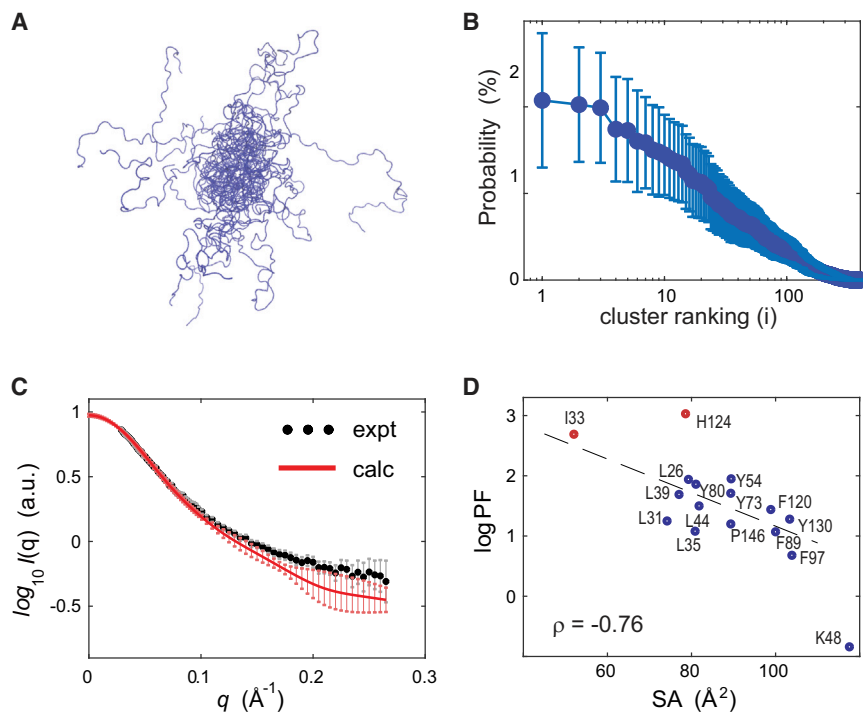
A

B

C

D

Figure 4. Ensemble-Structure Construction for the Native Compact-Disordered NTD

(A) Ensemble-structures constructed by integrating SAXS and FP-PF data. Shown is the ensemble of the top ten structures.

(B) Probability distribution for the ensemble structures. The error bars were the standard deviations from nine sets of probability distributions calculated using a same set of conformations.

(C) Measured and calculated SAXS profiles. The calculated SAXS profile (in red) is the average of ensemble structures. The SAXS data were deposited into the SASBDB databank (https://www.sasbdb.org/data/SASDEE2).

(D) Measured logPF values and ensemble-based solvent-accessible surface areas (SAs). A set of 16 residue side chains were probed and shown.

in multi-technique modeling protein structures and protein-protein interactions has been demonstrated in our previous proof-of-principle studies (Huang et al., 2016) and more recently in the structure determination of a multidomain estrogen receptor complex (Huang et al., 2018). To measure FP-PF data, purified NTD samples were exposed to a focused synchrotron X-ray white beam, where radiolysis-generated hydroxyl radicals react with solvent-accessible side chains, and the sites and rates of oxidation are monitored by tandem MS (Takamoto and Chance, 2006). The extent of modification is quantified as a function of X-ray exposure time (see examples in Figure S2), yielding a measured rate of footprinting (k_{fp}) for each site. Dividing the measured rates by those expected for a full accessible site, the intrinsic reactivity with hydroxyl radical (k_R), provides a residue-specific PF (PF = k_R/k_{fp}) (Huang et al., 2015). The natural log of the PF values provides a quantitative residue-specific map on solvent accessibility; high logPF values reflect more protection from solvent (e.g., residues I33 and H124 with logPF = 2.69 and 3.03, respectively), while lower values (e.g., F97 with logPF = 0.68) reflect greater solvent accessibility. Table S3 shows the log PF values for the set of 16 residues that were quantitatively analyzed after Lys-C/Asp-N and/or pepsin digestions. These footprinting protection factor (FP-PF) data provide information about solvent accessibility at the various sites that can be integrated with SAXS data to facilitate ensemble-structure construction for the natively compact-disordered NTD.

We used a maximum-likelihood method for ensemble-structure construction that makes use of a structural library of NTD conformations in conjunction with SAXS and FP-PF data, following the general approaches available in the literature (Bernado et al., 2005; Borgia et al., 2016; Brookes and Head-Gordon, 2016; Roux and Weare, 2013; Rozycki et al., 2011; Schwalbe et al., 2014). To generate the conformational library, various

computational methods ranging from coarse-grained to simplified all-atom models have been developed (Ghavami et al., 2013; Krzeminski et al., 2013; Ozenne et al., 2012; Vitalis and Pappu, 2009; Zhang and Chen, 2014). Due to the prior knowledge about the NTD compactness, here we used an accumulative set of 35-μs all-atom explicit-solvent molecular dynamics (MD) simulation trajectories (Methods). The resulting pool of NTD conformations is combined with and compared against experimental SAXS and FP-PF data simultaneously to construct the best-fit ensemble-structures. The goodness of fit between the ensemble-calculated and experiment data is assessed by two unit-less functions χ^2 (Equation 1) and φ^2 (Equation 2), each measuring the difference between calculated and experimental SAXS and FP-PF data, respectively (Huang et al., 2018). To avoid potential overfitting, we applied a maximum-likelihood method (Equations 3 and 4, and Figure S3). As such, a broad probability distribution$\{P_i\}$ is determined for the ensemble-structures. It is clear that while the MD simulations were able to sample a broad range of conformations (e.g., with a wide R_g distribution; Figure S4A), the ensemble fitting against experimental SAXS and FP-PF data only selects a subset of sampled conformations that better match experimental SAXS and footprinting-related SA values (Figure S4B). Overall, this multi-technique modeling for the NTD resulted in an ensemble of top 10 clusters of structures (Figure 4A) that contributes to a total of 16% of the entire population and an ensemble of top 100 structures that accounts for about 80% of the population (Figure 4B).

Comparison of the ensemble-calculated and experimental SAXS profiles shows a reasonably good agreement (χ^2 = 1.7 as defined in Equation 1; see Figure 4C). In addition, a weighted average for side-chain solvent-accessible surface area (SA) is estimated for each residue and plotted against its corresponding logPF value (Figure 4D). The SA versus logPF plot has a correlation coefficient of −0.76 (p value = 6.3 × 10^{-4} for the set of 16 residues), suggesting reasonable agreement between the derived ensemble-structures and experimental footprinting data. Previous correlation analyses of this kind have been

performed on globular folded proteins, which typically exhibit a wide range of logPF values. However, most of the observations here have logPF values from 1 to 2 (SA values of 80–110 Å^2), and have few values at the extremes of being either highly solvent-protected or highly solvent-accessible (e.g., upper left or lower right quadrants). In order to remove any potential bias due to residue size, we normalized the SA data into the fractional SA (fSA) values, using the maximum possible SA for the residue (Tien et al., 2013). In a re-plotted fSA versus logPF in Figure S5, 12 out of the 16 points (circled) are clustered in the "middle" of the plot in a restricted range. This contrasts with globular folded proteins that exhibit as many residues in the "middle" range as in the high/low fSA regions (Gustavsson et al., 2017; Kaur et al., 2015). This is presumably because the existence of a balanced distribution, including both high (e.g., fSA >0.8) and low (e.g., fSA <0.4) solvent-accessible residues, correlates with structural stability and maintains the overall fold for globular folded proteins. By comparison, the majority of NTD residues are in an intermediate range of fSA (and logPF) values, consistent with its dynamic but compact nature. This relatively narrow fSA distribution is also consistent with the modest chemical shift dispersion observed in NMR spectra and may reflect a structural signature of this NTD. Retrospectively, this broad distribution for the ensemble is also consistent with the typical behavior of disordered proteins, where an ensemble of structures is often required to characterize the structural properties of IDPs.

We next performed an ensemble contact map analysis for the NTD ensemble-structures (STAR Methods). The resulting contact map shows that the NTD has multiple medium and long-range contacts formed (within residues 11–75), pointing to a "collapsed" segment (for a portion of the distribution) at its N-terminus, compared to its C-terminus (Figure 5A). This regional collapse is consistent with the higher hydrophobicity of its N-terminal sequence than the C-terminal (Figure 2A). Moreover, long-range interactions are formed (e.g., frequently observed in the ensemble) between two, five-residue peptides, each centered at I33 and S118 (marked by an arrow in Figure 5A and illustrated in Figure 5B). Residue I33 is predicted to have an SA value of 52 Å^2 from the ensemble-structures (Table S3), indicating that I33 is more protected from solvent exposure than the typical or average member of the ensemble. To gain insight into the nature of these conformations and their distributions, we examined the explicit structural distribution of I33, compared with L44, which has a similar/compatible side-chain size but with a higher SA value indicating much greater solvent exposure. It can be seen that based on the top 100 structures (Figure 5C), I33 has far more ensemble members with SA values below 50 Å^2, compared with L44 that has a greater number of conformations above 100 Å^2. I33 is on average solvent-protected to a greater degree, presumably due to its "metastable" interaction with S118 (see below) that tilts the conformational distribution toward greater protection, compared with L44. Although the interaction itself is presumably relatively weak compared with tertiary contacts for a globular well-folded protein, the metastable nature of this long-range interaction could provide a critical structural role driving the function of the NTD (Wright and Dyson, 2015).

To examine the functional role of S118 and to test its structural interaction predicted by our ensemble-structures, we mutated the non-charged S118 residue to a charged residue Asp (D)

(i.e., S118D), as a phosphomimetic mutation. The ellipticity at 222 nm shows that S118D increases the content of ordered secondary structure (Figure 5D). To gain insight into the impact on the overall protein, we further acquired SAXS data for the S118D mutant, yielding the R_g^{expt} value of 38.7 Å (Figures 5E and S6), which is greater than that of the wild-type (WT) (R_g^{expt} = 31.0 Å) and smaller than the denatured state (R_g^{expt} = 43.4 Å for the NTD in the presence of 6 M GdnHCl). Mutation-dependent conformational changes are also confirmed by peak shifts and appearance/disappearance in the ^{1}H-^{15}N TROSY spectra of S118D (Figure 5F; arrows). While detailed NMR assignments to identify specific residues involved will be the subject of future studies, these considerable changes involving at least 12 spectrum peaks indicate that S118D mutation leads to modest conformational changes that spread out well beyond the mutation site itself, in accord with the sizable R_g change as observed by SAXS. Overall, these data collectively show that the mutation propagates its structural impact and physically extends the polypeptide chain, presumably by destabilizing S118-mediated long-range contacts, while counterintuitively resulting in a gain of local secondary structure.

We also examined the impact of the S118D mutation on the NTD binding to TBP, a general transcription factor TATA box-binding protein, known as an ER coactivator in the transcriptional machinery (Louder et al., 2016; Sadovsky et al., 1995). We estimated a weak-to-modest binding affinity of 53 ± 12 μM between the WT NTD and TBP, using surface plasmon resonance (SPR) spectrometry (Figure 6A), consistent with the previously reported binding affinity in the micromolar range (Warnmark et al., 2001). The NTD-TBP binding is further demonstrated by NMR experiments, which show more than 15 peak shifts and appearance/disappearance in the ^{1}H-^{15}N spectra of the WT upon addition of TBP (Figure S7A). Compared with the WT, however, the addition of TBP leads to a greater extent of changes in the ^{1}H-^{15}N spectra of the S118D mutant, with a set of 23 peak changes (Figure S7B; arrows), indicating that S118D increases coactivator binding as a result of the conformational changes. This increased coactivator binding is further supported by the SPR measurements, where S118D increases the TBP binding affinity more than 10-fold to K_d = 3.9 ± 0.4 μM (Figure 6B), compared with the WT's K_d = 53 ± 12 μM. Together, these data show that the S118D mutation induces sizable conformational changes within the NTD and further increases the coactivator binding.

Metastable Contact in the IDP Validated by ^{19}F NMR

To test the validity of the proposed I33-S118 interaction, we conducted ^{19}F NMR studies on the NTD by introducing a cysteine residue at the location of S118 to allow covalently linked ^{19}F labeling with a trifluoromethyl (-CF$_3$) group (depicted in Figures 7A and 7B). The ^{19}F labeling was achieved using 3-bromo-1,1,1-trifluoroacetone (BTFA), a widely used labeling reagent in ^{19}F NMR studies of both disordered and well-folded proteins (Didenko et al., 2013; Kitevski-LeBlanc and Prosser, 2012; Li et al., 2010; Matei and Gronenborn, 2016), with a more recent application to the nuclear receptor PPARγ (Chrisman et al., 2018). Hereafter, we refer to the BTFA-labeled NTD S118C protein variant as NTD^{S118C}-BTFA. Because there is no cysteine in the native NTD, ^{19}F NMR spectra of the NTD^{S118C}-BTFA yielded a single peak in each ^{19}F NMR spectrum (Figure 7C,
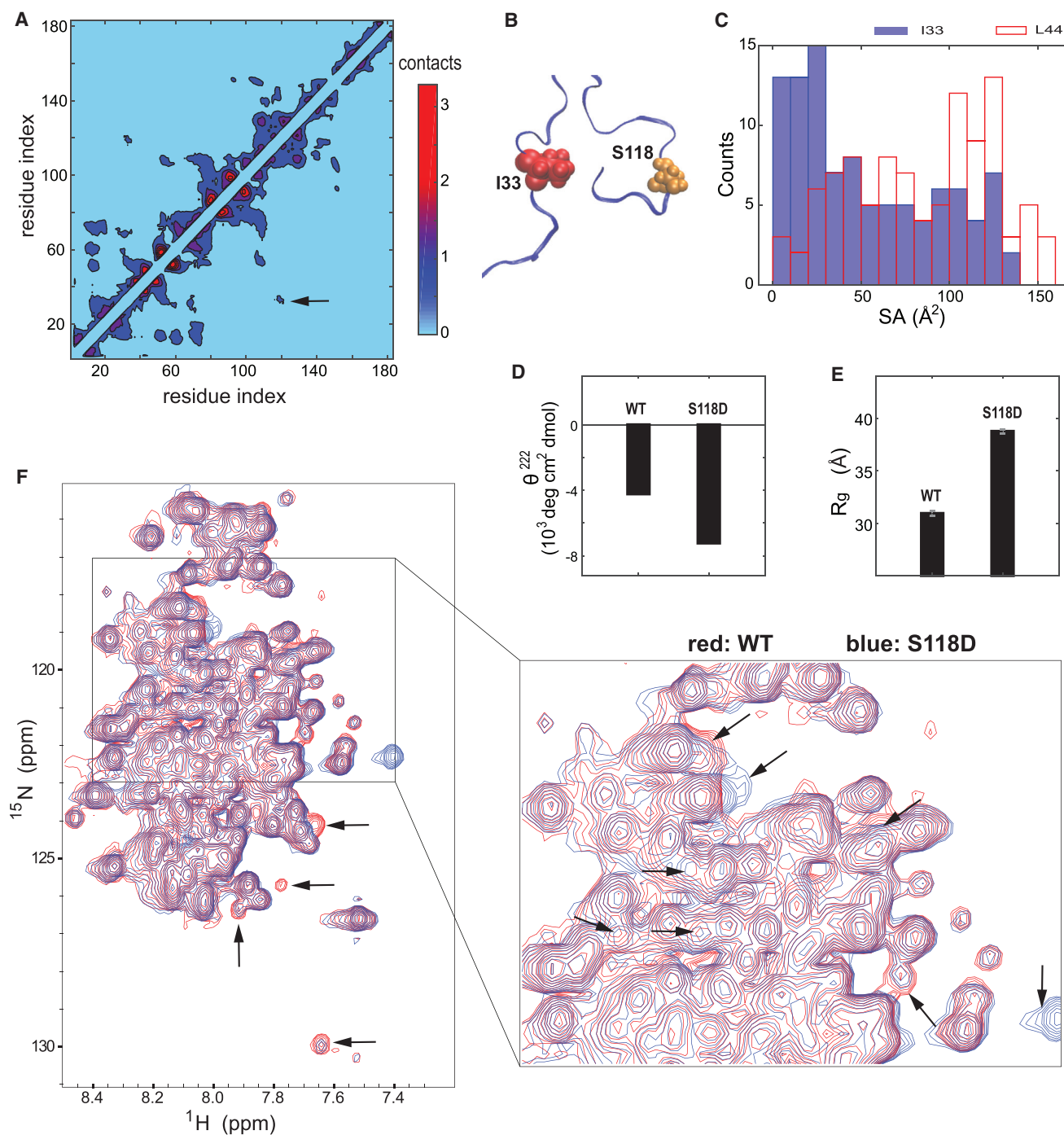
Figure 5. Ensemble-Contact Map and Mutation-Induced Conformational Changes

(A) Contact map shows that the N-terminal region of the NTD (e.g., residues 11–75). has more contacts formed than its C-terminal region. The color bar indicates the contact number, where each contact is ensemble weighted (STAR Methods). The metastable I33-S118 contact is marked by an arrow, where three of the top ten structures from the ensemble make the contact.

(B) Cartoon illustration of I33-S118 interaction.

(C) Histogram for SA values for residues I33 and L44 from top 100 structures of the ensemble.

(D) CD signal at 222 nm for S118D as well as WT.

(E) The R_g value of 38.7 ± 0.2 Å for mutation S118D, compared with the R_g value of 31.0 ± 0.2 Å for the WT. Related SAXS data shown in Figure S6.

(F) Overlap of ^{1}H-^{15}N TROSY spectra between WT (red) and mutant S118D (blue). Peak changes/shifts marked by arrows.
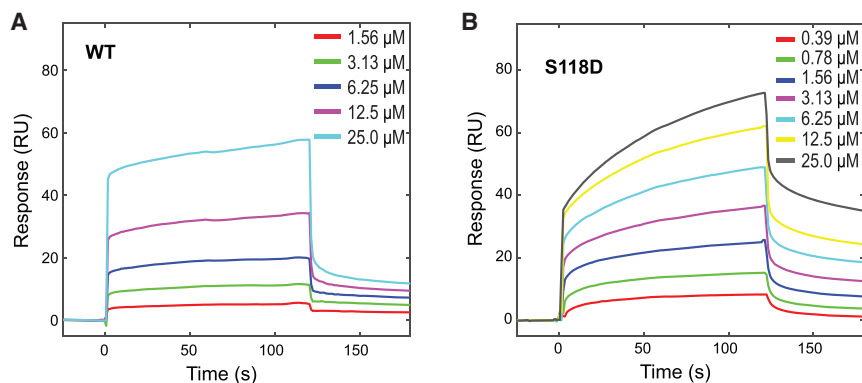
Figure 6. Alternation of TBP Binding upon S118D Mutation

(A) Binding of NTD with TBP measured by SPR spectrometry. An apparent binding affinity was estimated at $K_d = 53 \pm 12$ μM.

(B) Measured TBP binding for the S118D mutant using SPR spectrometry. An apparent binding affinity was estimated at $K_d = 3.9 \pm 0.4$ μM.

left). Of note, the relative exposure to the solvent of the BTFA probe can be qualitatively determined by the ^{19}F peak shift as a function of D_2O concentration, an effect known as D_2O-sovlent induced isotope shift (Chrisman et al., 2018; Kitevski-LeBlanc and Prosser, 2012). Here, the "wild-type" form of the NTD^{S118C}-BTFA was observed with a peak shift $\Delta\delta$ of 7.5×10^{-2} ppm between 10% and 50% D_2O. We next determined the effect of mutations near residue I33 via two mutations: a single-point mutation of L31A and a triple mutation of K32A/I33A/P34A. The ^{19}F NMR spectra of the L31A showed a negligible difference in the peak shift $\Delta\delta$, compared with the WT NTD^{S118C}-BTFA (Figure 7C, middle). In contrast to L31A, as a negative control, the triple mutant K32A/I33A/P34A was observed with a $\Delta\delta$ value of 9.2×10^{-2} ppm (Figure 7C, right), which is a 23% increase from the WT. Of note, while the D_2O itself causes a small chemical shift, the focus here is on the $\Delta\delta$ difference between 10% and 50% D_2O, as opposed to the absolute chemical shift with a specific D_2O-concentration buffer. Given the large sequence separation between I33 and S118, the K32A/I33A/P34A mutations are observed with an unexpectedly impact on the surroundings of residue S118. These ^{19}F NMR data of the WT and the triple mutant provide a strong evidence that the mutations disrupt the I33-S118 contact, thereby increasing the solvent exposure of the ^{19}F probe at residue S118. Given a wide range of conformations available for the IDP and the metastability of the long-range contact, it is difficult for a majority of biophysical techniques to achieve a validity test on such transient contacts. Here, the one-dimensional ^{19}F NMR spectroscopy, due in part to the natural abundance of fluorine-19, offers a highly sensitive tool to detect subtle changes associated with the NTD contact. As such, our ^{19}F NMR data together with site-directed mutagenesis studies confirm the proposed metastable contact between residues I33 and S118 of the NTD ensemble.

DISCUSSION

The NTD accounts for a large portion of the total transcriptional activities of most nuclear receptors in terms of transactivation function. While it was recognized early on that ERα-NTD is structurally disordered, little is known about its molecular details, compared with extensive knowledge available for other regions of the receptor, such as the DNA-binding domain and the hormone-binding domain (Figure 1A). This study provides a comprehensive characterization of the rather distinctive structural features of NTDs for both native and chemically denatured states.

Our biophysical measurements show that the NTD is mostly disordered as revealed by CD and NMR, although SAXS data point to considerable compactness, in accord with the modest hydrophobicity and nearly zero net charge that is more common for globular proteins. The ensemble-structures were observed to undergo a loss of residual secondary structure and a structural expansion from a narrow single-peak distance distribution in the native state to a broad distribution in chemically denatured states, indicative of melting of pre-existing structural features associated with the compactness and/or helicity. Of note, this phenomenon of a large expansion with >40% increase in R_g from 31 to 43 Å was observed for ERα-NTD only; a generalization to and comparison with other IDPs, such as RXRα-NTD and AR-NTD, has not yet been attempted.

The ensemble-structures constructed by multi-technique modeling, which combines SAXS and FP-PF data together with a library of simulation-generated conformations, provide a rare opportunity to observe the molecular details of ERα-NTD. We acknowledge that this modeling process cannot provide a unique solution to understanding the ERα-NTD structures in part due to the ensemble-average and/or conformer-coexistence nature of both SAXS and FP-PF data (i.e., footprinting-based PFs). We further note that several residues had extreme logPF values not explained by the modeling. In particular, H124 was observed to be the most protected, but our ensemble-structure models could not explain its high degree of solvent protection (Figure 4D), which points to next-steps for future ensemble refinements. Nonetheless, given the strong evidence that validates our constructed ensemble-structures for ERα-NTD, our multi-technique approach could be applied for the structure determination of other IDP systems such as RXRα-NTD.

In a broader context, IDPs are increasingly appreciated as functionally important for coactivator recruitment of protein-protein interactions involved in cellular signaling and transcriptional regulation. Typical IDPs are viewed as a diverse population of interchangeable structures or conformers that coexist in a concerted equilibrium. Here, the ensemble-structure studies for ERα-NTD add to our understanding of the range of the structure-function capability of IDPs. A large portion of the ensemble population for ERα-NTD favors a regional collapse at the N-terminus contributing to the overall compactness. Moreover, a subset of the population, roughly three out of the top 10 structures in the ensemble, adopt long-range contacts near I33 and S118 that presumably tilt the dynamic equilibrium in favor of more compact conformers. The extended NTD ensemble, accompanied by the increase of ordered secondary structure, possesses structural elements or flexibility that permits the IDP to interact more productively with the folded TBP
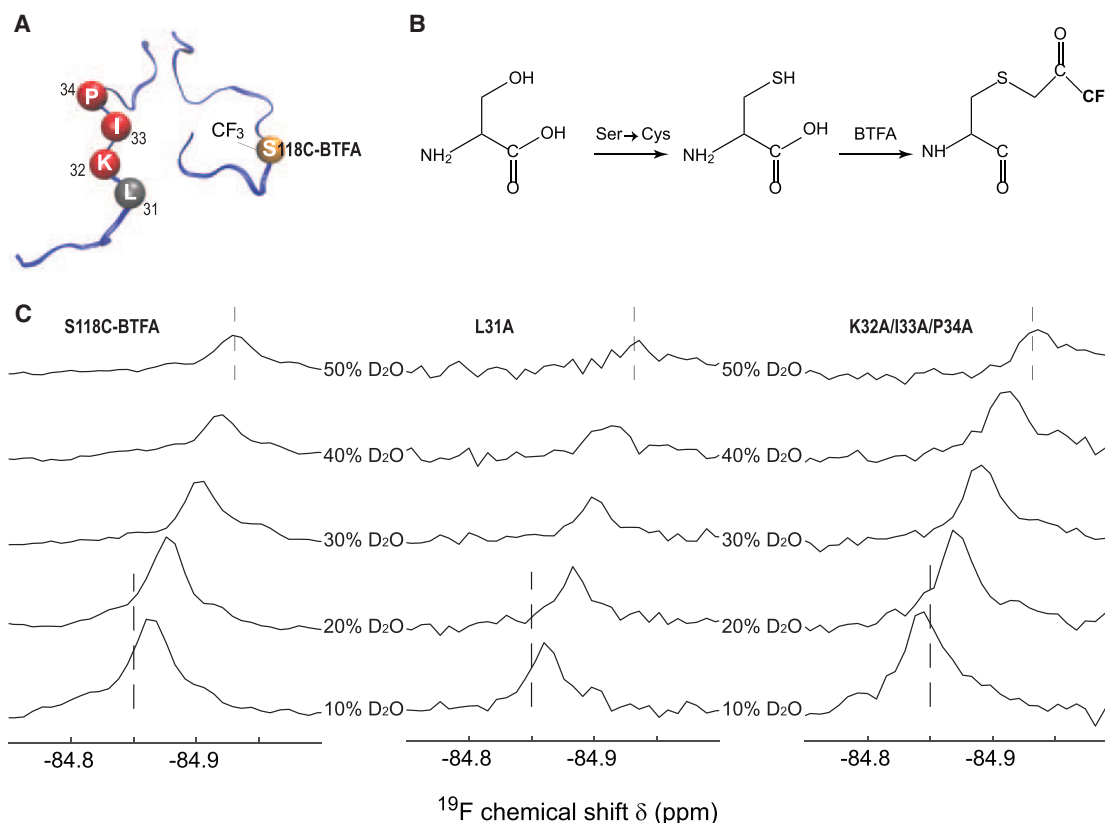
Figure 7. Mutations Near Residue I33 Alter the Fluorine-19 Chemical Shift at Residue S118

(A) Location of the BTFA (3-bromo-1,1,1-trifluoroacetone) at S118. Sites of mutation near I33 (the point mutation L31A and the triple mutation K32A/I33A/P34A) are also labeled.

(B) Schematic of the NTD^{S118C}-BTFA labeling where fluorine-19 (-CF$_3$ group) is covalently linked to the cysteine of mutant S118C in a one-step chemical reaction.

(C) ^{19}F NMR spectra of the WT, L31A, and K32A/I33A/P34A of the NTD^{S118C}-BTFA under different D$_2$O concentrations. Compared with the WT NTD^{S118C}-BTFA, ^{19}F chemical shifts are observed with a negligible change for mutant L31A, but with a 23% increase for the K32A/I33A/P34A (between 10% and 50% D$_2$O), as a result of the effect of D$_2$O-solvent induced isotope shift. Dash lines were used for visualization only.

protein, resulting in stronger coactivator binding. Functionally, S118 is a known phosphorylation site that modulates the receptor's transcriptional activity (Chen et al., 2000), and an increase in the level of S118 phosphorylation has been associated with endocrine resistance via direct recruitment of coactivators (Kato et al., 1995). As a phosphomimetic mutation, S118D directly links a phosphorylation-driven shift in the NTD conformational equilibrium in favor of coactivator recruitment, suggesting the role of residue S118 as a "structural inhibitor" and further providing a molecular basis for understanding S118-associated endocrine resistance in breast cancer. S118 phosphorylation is also critical for association with a *cis/trans* isomerase pin1 as observed in a truncated NTD segment, while mutation of S118 to alanine prevents the association (Rajbhandari et al., 2012). Such mutation-induced modulation is also observed in other IDPs, such as the transcription factor HIF-1α transactivation domain (Berlow et al., 2017) and a disordered PAGE4 protein (Kulkarni et al., 2017). More strikingly, despite the "metastable" nature of the I33-S118 contact, mutation near residue I33 considerably alters the ^{19}F chemical shifts at the position of S118C at a distance along the amino acid sequence, thereby confirming the structural articulation of this long-range contact

observed in the IDP ensemble-structures. Because there exists a wide range of conformations for the IDP and it is difficult to directly visualize any ensemble-averaged features of these conformations, our contact map analysis enables an ensemble-structure approach for studying disordered proteins by making testable predictions on the I33-S118 contact being the case in point. In conclusion, as we note above that the hydrophobicity and mean net charge of RXRα-NTD is similar to that of ERα-NTD, our findings suggest that a comprehensive characterization of RXRα-NTD and/or other NTDs by these approaches may reveal additional examples of metastable contacts in the context of IDPs that fine-tune the conformational equilibrium to execute particular molecular functions as a general mechanism of mediating nuclear receptor structure and function.

STAR★METHODS

Detailed methods are provided in the online version of this paper and include the following:

- KEY RESOURCES TABLE
- CONTACT FOR REAGENT AND RESOURCE SHARING

- **METHOD DETAILS**
  - Plasmid Construct
  - Protein Expression and Purification
  - Circular Dichroism Spectroscopy
  - Two-Dimensional NMR Spectroscopy
  - Small-Angle X-Ray Scattering
  - Amide Hydrogen Exchange with Mass Spectrometry
  - Hydroxyl Radical Protein Footprinting and Protection Factor Analysis
  - Conformational Library
  - Ensemble Structure Construction
  - Ensemble Contact Map
  - Surface Plasmon Resonance
  - Fluorine-19 NMR Spectroscopy
- **QUANTIFICATION AND STATISTICAL ANALYSIS**
- **DATA AND SOFTWARE AVAILABILITY**

SUPPLEMENTAL INFORMATION

Supplemental Information includes seven figures and three tables and can be found with this article online at https://doi.org/10.1016/j.str.2018.10.026.

AUTHOR CONTRIBUTIONS

S.Y. designed the research. Y.P., A.H., S.K., and Z.D. expressed and purified the proteins. Y.P. performed CD experiments. S.C., Y.P., and M.B. contributed to 2D NMR experiments. X.X., Y.P., Z.D., and W.K.S. contributed to H/D exchange experiments. S.Y., W.S., and L.Y. collected scattering data. J.K., Y.P., M.R.C., and S.Y. contributed to footprinting experiments and analyses. W.J. and S.Y. performed MD simulations. S.Y. performed multi-technique modeling. W.Z. contributed to SAXS-based R_g analyses. Y.P. and Y.C. performed SPR. Y.P., P.A., and Z.D. contributed to 1D ^{19}F NMR experiments. All authors edited the manuscript.

DECLARATION OF INTERESTS

The authors declare no competing interests.

REFERENCES

Bai, Y., Milne, J.S., Mayne, L., and Englander, S.W. (1993). Primary structure effects on peptide group hydrogen exchange. Proteins 17, 75–86.

Belorusova, A., Osz, J., Petoukhov, M.V., Peluso-Iltis, C., Kieffer, B., Svergun, D.I., and Rochel, N. (2016). Solution behavior of the intrinsically disordered N-terminal domain of retinoid X receptor alpha in the context of the full-length protein. Biochemistry 55, 1741–1748.

Berlow, R.B., Dyson, H.J., and Wright, P.E. (2017). Hypersensitive termination of the hypoxic response by a disordered protein switch. Nature 543, 447–451.

Bernado, P., Blanchard, L., Timmins, P., Marion, D., Ruigrok, R.W., and Blackledge, M. (2005). A structural model for unfolded proteins from residual dipolar couplings and small-angle x-ray scattering. Proc. Natl. Acad. Sci. U S A 102, 17002–17007.

Bernado, P., and Svergun, D.I. (2012). Structural analysis of intrinsically disordered proteins by small-angle X-ray scattering. Mol. Biosyst. 8, 151–167.

Best, R.B., Zheng, W., and Mittal, J. (2014). Balanced protein-water interactions improve properties of disordered proteins and non-specific protein association. J. Chem. Theory Comput. 10, 5113–5124.

Boomsma, W., Ferkinghoff-Borg, J., and Lindorff-Larsen, K. (2014). Combining experiments and simulations using the maximum entropy principle. PLoS Comput. Biol. 10, e1003406.

Borgia, A., Zheng, W., Buholzer, K., Borgia, M.B., Schuler, A., Hofmann, H., Soranno, A., Nettels, D., Gast, K., Grishaev, A., et al. (2016). Consistent view of polypeptide chain expansion in chemical denaturants from multiple experimental methods. J. Am. Chem. Soc. 138, 11714–11726.

Brookes, D.H., and Head-Gordon, T. (2016). Experimental inferential structure determination of ensembles for intrinsically disordered proteins. J. Am. Chem. Soc. 138, 4530–4538.

Buck, M., Radford, S.E., and Dobson, C.M. (1994). Amide hydrogen exchange in a highly denatured state. Hen egg-white lysozyme in urea. J. Mol. Biol. 237, 247–254.

Chen, D., Riedl, T., Washbrook, E., Pace, P.E., Coombes, R.C., Egly, J.M., and Ali, S. (2000). Activation of estrogen receptor alpha by S118 phosphorylation involves a ligand-dependent interaction with TFIIH and participation of CDK7. Mol. Cell 6, 127–137.

Choy, W.Y., and Forman-Kay, J.D. (2001). Calculation of ensembles of structures representing the unfolded state of an SH3 domain. J. Mol. Biol. 308, 1011–1032.

Chrisman, I.M., Nemetchek, M.D., de Vera, I.M.S., Shang, J., Heidari, Z., Long, Y., Reyes-Caballero, H., Galindo-Murillo, R., Cheatham, T.E., 3rd, Blayo, A.L., et al. (2018). Defining a conformational ensemble that directs activation of PPARgamma. Nat. Commun. 9, 1794.

Conn, A.R., Gould, N., and Toint, P.L. (1997). A globally convergent Lagrangian barrier algorithm for optimization with general inequality constraints and simple bounds. Math. Comput. 66, 261–288.

Craig, P.O., Latzer, J., Weinkam, P., Hoffman, R.M., Ferreiro, D.U., Komives, E.A., and Wolynes, P.G. (2011). Prediction of native-state hydrogen exchange from perfectly funneled energy landscapes. J. Am. Chem. Soc. 133, 17463–17472.

Das, R.K., and Pappu, R.V. (2013). Conformations of intrinsically disordered proteins are influenced by linear sequence distributions of oppositely charged residues. Proc. Natl. Acad. Sci. U S A 110, 13392–13397.

Dawson, R., Muller, L., Dehner, A., Klein, C., Kessler, H., and Buchner, J. (2003). The N-terminal domain of p53 is natively unfolded. J. Mol. Biol. 332, 1131–1141.

De Mol, E., Fenwick, R.B., Phang, C.T., Buzon, V., Szulc, E., de la Fuente, A., Escobedo, A., Garcia, J., Bertoncini, C.W., Estebanez-Perpina, E., et al. (2016). EPI-001, a compound active against castration-resistant prostate cancer, targets transactivation unit 5 of the androgen receptor. ACS Chem. Biol. 11, 2499–2505.

De Mol, E., Szulc, E., Di Sanza, C., Martinez-Cristobal, P., Bertoncini, C.W., Fenwick, R.B., Frigole-Vivas, M., Masin, M., Hunter, I., Buzon, V., et al. (2018). Regulation of androgen receptor activity by transient interactions of its transactivation domain with general transcription regulators. Structure 26, 145–152.e3.

Delaglio, F., Grzesiek, S., Vuister, G.W., Zhu, G., Pfeifer, J., and Bax, A. (1995). NMRPipe: a multidimensional spectral processing system based on UNIX pipes. J. Biomol. NMR 6, 277–293.

Didenko, T., Liu, J.J., Horst, R., Stevens, R.C., and Wuthrich, K. (2013). Fluorine-19 NMR of integral membrane proteins illustrated with studies of GPCRs. Curr. Opin. Struct. Biol. 23, 740–747.

Englander, S.W., and Kallenbach, N.R. (1983). Hydrogen exchange and structural dynamics of proteins and nucleic acids. Q. Rev. Biophys. 16, 521–655.

Fuertes, G., Banterle, N., Ruff, K.M., Chowdhury, A., Mercadante, D., Koehler, C., Kachala, M., Estrada Girona, G., Milles, S., Mishra, A., et al. (2017).

Decoupling of size and shape fluctuations in heteropolymeric sequences reconciles discrepancies in SAXS vs. FRET measurements. Proc. Natl. Acad. Sci. U S A *114*, E6342–E6351.

Ganguly, D., and Chen, J. (2009). Structural interpretation of paramagnetic relaxation enhancement-derived distances for disordered protein states. J. Mol. Biol. *390*, 467–477.

Ghavami, A., van der Giessen, E., and Onck, P.R. (2013). Coarse-grained potentials for local interactions in unfolded proteins. J. Chem. Theory Comput. *9*, 432–440.

Gustavsson, M., Wang, L., van Gils, N., Stephens, B.S., Zhang, P., Schall, T.J., Yang, S., Abagyan, R., Chance, M.R., Kufareva, I., et al. (2017). Structural basis of ligand interaction with atypical chemokine receptor 3. Nat. Commun. *8*, 14135.

Hornak, V., Abel, R., Okur, A., Strockbine, B., Roitberg, A., and Simmerling, C. (2006). Comparison of multiple Amber force fields and development of improved protein backbone parameters. Proteins *65*, 712–725.

Hsieh, A., Lu, L., Chance, M.R., and Yang, S. (2017). A practical guide to iSPOT modeling: an integrative structural biology platform. Adv. Exp. Med. Biol. *1009*, 229–238.

Huang, J., and MacKerell, A.D., Jr. (2018). Force field development and simulations of intrinsically disordered proteins. Curr. Opin. Struct. Biol. *48*, 40–48.

Huang, J., Rauscher, S., Nawrocki, G., Ran, T., Feig, M., de Groot, B.L., Grubmuller, H., and MacKerell, A.D., Jr. (2017). CHARMM36m: an improved force field for folded and intrinsically disordered proteins. Nat. Methods *14*, 71–73.

Huang, W., Peng, Y., Kiselar, J., Zhao, X., Albaqami, A., Mendez, D., Chen, Y., Chakravarthy, S., Gupta, S., Ralston, C., et al. (2018). Multidomain architecture of estrogen receptor reveals interfacial cross-talk between its DNA-binding and ligand-binding domains. Nat. Commun. *9*, 3520.

Huang, W., Ravikumar, K.M., Chance, M.R., and Yang, S. (2015). Quantitative mapping of protein structure by hydroxyl radical footprinting-mediated structural mass spectrometry: a protection factor analysis. Biophys. J. *108*, 107–115.

Huang, W., Ravikumar, K.M., Parisien, M., and Yang, S. (2016). Theoretical modeling of multiprotein complexes by iSPOT: integration of small-angle X-ray scattering, hydroxyl radical footprinting, and computational docking. J. Struct. Biol. *196*, 340–349.

Jo, S., and Jiang, W. (2015). A generic implementation of replica exchange with solute tempering (REST2) algorithm in NAMD for complex biophysical simulations. Comput. Phys. Commun. *197*, 304–311.

Kato, S., Endoh, H., Masuhiro, Y., Kitamoto, T., Uchiyama, S., Sasaki, H., Masushige, S., Gotoh, Y., Nishida, E., Kawashima, H., et al. (1995). Activation of the estrogen receptor through phosphorylation by mitogen-activated protein kinase. Science *270*, 1491–1494.

Kaur, P., Kiselar, J., Yang, S., and Chance, M.R. (2015). Quantitative protein topography analysis and high-resolution structure prediction using hydroxyl radical labeling and tandem-ion mass spectrometry (MS). Mol. Cell Proteomics *14*, 1159–1168.

Kitevski-LeBlanc, J.L., and Prosser, R.S. (2012). Current applications of 19F NMR to studies of protein structure and dynamics. Prog. Nucl. Magn. Reson. Spectrosc. *62*, 1–33.

Kohn, J.E., Millett, I.S., Jacob, J., Zagrovic, B., Dillon, T.M., Cingel, N., Dothager, R.S., Seifert, S., Thiyagarajan, P., Sosnick, T.R., et al. (2004). Random-coil behavior and the dimensions of chemically unfolded proteins. Proc. Natl. Acad. Sci. U S A *101*, 12491–12496.

Krzeminski, M., Marsh, J.A., Neale, C., Choy, W.Y., and Forman-Kay, J.D. (2013). Characterization of disordered proteins with ENSEMBLE. Bioinformatics *29*, 398–399.

Kulkarni, P., Jolly, M.K., Jia, D., Mooney, S.M., Bhargava, A., Kagohara, L.T., Chen, Y., Hao, P., He, Y., Veltri, R.W., et al. (2017). Phosphorylation-induced conformational dynamics in an intrinsically disordered protein and potential role in phenotypic heterogeneity. Proc. Natl. Acad. Sci. U S A *114*, E2644–E2653.

Kumar, R., Moure, C.M., Khan, S.H., Callaway, C., Grimm, S.L., Goswami, D., Griffin, P.R., and Edwards, D.P. (2013). Regulation of the structurally dynamic

N-terminal domain of progesterone receptor by protein-induced folding. J. Biol. Chem. *288*, 30285–30299.

Kumar, R., and Thompson, E.B. (2012). Folding of the glucocorticoid receptor N-terminal transactivation function: dynamics and regulation. Mol. Cell. Endocrinol. *348*, 450–456.

Kyte, J., and Doolittle, R.F. (1982). A simple method for displaying the hydropathic character of a protein. J. Mol. Biol. *157*, 105–132.

Lavery, D.N., and McEwan, I.J. (2005). Structure and function of steroid receptor AF1 transactivation domains: induction of active conformations. Biochem. J. *391*, 449–464.

Lee, C.W., Martinez-Yamout, M.A., Dyson, H.J., and Wright, P.E. (2010). Structure of the p53 transactivation domain in complex with the nuclear receptor coactivator binding domain of CREB binding protein. Biochemistry *49*, 9964–9971.

Li, C.G., Wang, G.F., Wang, Y.Q., Creager-Allen, R., Lutz, E.A., Scronce, H., Slade, K.M., Ruf, R.A.S., Mehl, R.A., and Pielak, G.J. (2010). Protein F-19 NMR in *Escherichia coli*. J. Am. Chem. Soc. *132*, 321–327.

Li, J., Motlagh, H.N., Chakuroff, C., Thompson, E.B., and Hilser, V.J. (2012). Thermodynamic dissection of the intrinsically disordered N-terminal domain of human glucocorticoid receptor. J. Biol. Chem. *287*, 26777–26787.

Lindorff-Larsen, K., Kristjansdottir, S., Teilum, K., Fieber, W., Dobson, C.M., Poulsen, F.M., and Vendruscolo, M. (2004). Determination of an ensemble of structures representing the denatured state of the bovine acyl-coenzyme a binding protein. J. Am. Chem. Soc. *126*, 3291–3299.

Louder, R.K., He, Y., Lopez-Blanco, J.R., Fang, J., Chacon, P., and Nogales, E. (2016). Structure of promoter-bound TFIID and model of human pre-initiation complex assembly. Nature *531*, 604–609.

Mao, A.H., Crick, S.L., Vitalis, A., Chicoine, C.L., and Pappu, R.V. (2010). Net charge per residue modulates conformational ensembles of intrinsically disordered proteins. Proc. Natl. Acad. Sci. U S A *107*, 8183–8188.

Matei, E., and Gronenborn, A.M. (2016). (19)F Paramagnetic relaxation enhancement: a valuable tool for distance measurements in proteins. Angew. Chem. Int. Ed. *55*, 150–154.

Metivier, R., Petit, F.G., Valotaire, Y., and Pakdel, F. (2000). Function of N-terminal transactivation domain of the estrogen receptor requires a potential alpha-helical structure and is negatively regulated by the A domain. Mol. Endocrinol. *14*, 1849–1871.

Miao, Y., Feher, V.A., and McCammon, J.A. (2015). Gaussian accelerated molecular dynamics: unconstrained enhanced sampling and free energy calculation. J. Chem. Theory Comput. *11*, 3584–3595.

Myung, J.K., Banuelos, C.A., Fernandez, J.G., Mawji, N.R., Wang, J., Tien, A.H., Yang, Y.C., Tavakoli, I., Haile, S., Watt, K., et al. (2013). An androgen receptor N-terminal domain antagonist for treating prostate cancer. J. Clin. Invest. *123*, 2948–2960.

Nerenberg, P.S., and Head-Gordon, T. (2018). New developments in force fields for biomolecular simulations. Curr. Opin. Struct. Biol. *49*, 129–138.

Oldfield, C.J., and Dunker, A.K. (2014). Intrinsically disordered proteins and intrinsically disordered protein regions. Annu. Rev. Biochem. *83*, 553–584.

Ozenne, V., Bauer, F., Salmon, L., Huang, J.R., Jensen, M.R., Segard, S., Bernado, P., Charavay, C., and Blackledge, M. (2012). Flexible-meccano: a tool for the generation of explicit ensemble descriptions of intrinsically disordered proteins and their associated experimental observables. Bioinformatics *28*, 1463–1470.

Phillips, J.C., Braun, R., Wang, W., Gumbart, J., Tajkhorshid, E., Villa, E., Chipot, C., Skeel, R.D., Kale, L., and Schulten, K. (2005). Scalable molecular dynamics with NAMD. J. Comput. Chem. *26*, 1781–1802.

Piana, S., Donchev, A.G., Robustelli, P., and Shaw, D.E. (2015). Water dispersion interactions strongly influence simulated structural properties of disordered protein states. J. Phys. Chem. B *119*, 5113–5123.

Rajbhandari, P., Finn, G., Solodin, N.M., Singarapu, K.K., Sahu, S.C., Markley, J.L., Kadunc, K.J., Ellison-Zelski, S.J., Kariagina, A., Haslam, S.Z., et al. (2012). Regulation of estrogen receptor alpha N-terminus conformation and function by peptidyl prolyl isomerase Pin1. Mol. Cell. Biol. *32*, 445–457.

Ravikumar, K.M., Huang, W., and Yang, S. (2013). Fast-SAXS-pro: a unified approach to computing SAXS profiles of DNA, RNA, protein, and their complexes. J. Chem. Phys. *138*, 024112.

Riback, J.A., Bowman, M.A., Zmyslowski, A.M., Knoverek, C.R., Jumper, J.M., Hinshaw, J.R., Kaye, E.B., Freed, K.F., Clark, P.L., and Sosnick, T.R. (2017). Innovative scattering analysis shows that hydrophobic disordered proteins are expanded in water. Science *358*, 238–241.

Roux, B., and Weare, J. (2013). On the statistical equivalence of restrained-ensemble simulations with the maximum entropy method. J. Chem. Phys. *138*, 084107.

Rozycki, B., Kim, Y.C., and Hummer, G. (2011). SAXS ensemble refinement of ESCRT-III CHMP3 conformational transitions. Structure *19*, 109–116.

Russel, D., Lasker, K., Webb, B., Velazquez-Muriel, J., Tjioe, E., Schneidman-Duhovny, D., Peterson, B., and Sali, A. (2012). Putting the pieces together: integrative modeling platform software for structure determination of macromolecular assemblies. PLoS Biol. *10*, e1001244.

Sadovsky, Y., Webb, P., Lopez, G., Baxter, J.D., Fitzpatrick, P.M., Gizang-Ginsberg, E., Cavailles, V., Parker, M.G., and Kushner, P.J. (1995). Transcriptional activators differ in their responses to overexpression of TATA-box-binding protein. Mol. Cell. Biol. *15*, 1554–1563.

Sahu, D., Bastidas, M., and Showalter, S.A. (2014). Generating NMR chemical shift assignments of intrinsically disordered proteins using carbon-detected NMR methods. Anal. Biochem. *449*, 17–25.

Schwalbe, M., Ozenne, V., Bibow, S., Jaremko, M., Jaremko, L., Gajda, M., Jensen, M.R., Biernat, J., Becker, S., Mandelkow, E., et al. (2014). Predictive atomic resolution descriptions of intrinsically disordered hTau40 and alpha-synuclein in solution from NMR and small angle scattering. Structure *22*, 238–249.

Smirnovas, V., Baron, G.S., Offerdahl, D.K., Raymond, G.J., Caughey, B., and Surewicz, W.K. (2011). Structural organization of brain-derived mammalian prions examined by hydrogen-deuterium exchange. Nat. Struct. Mol. Biol. *18*, 504–506.

Smirnovas, V., Kim, J.I., Lu, X., Atarashi, R., Caughey, B., and Surewicz, W.K. (2009). Distinct structures of scrapie prion protein (PrPSc)-seeded versus spontaneous recombinant prion protein fibrils revealed by hydrogen/deuterium exchange. J. Biol. Chem. *284*, 24233–24241.

Sobolev, V., Sorokine, A., Prilusky, J., Abola, E.E., and Edelman, M. (1999). Automated analysis of interatomic contacts in proteins. Bioinformatics *15*, 327–332.

Song, D., Luo, R., and Chen, H.F. (2017). The IDP-specific force field ff14IDPSFF improves the conformer sampling of intrinsically disordered proteins. J. Chem. Inf. Model. *57*, 1166–1178.

Svergun, D., Barberato, C., and Koch, M.H.J. (1995). CRYSOL - a program to evaluate X-ray solution scattering of biological macromolecules from atomic coordinates. J. Appl. Crystallogr. *28*, 768–773.

Svergun, D.I. (1992). Determination of the regularization parameter in indirect-transform methods using perceptual criteria. J. Appl. Crystallogr. *25*, 495–503.

Takamoto, K., and Chance, M.R. (2006). Radiolytic protein footprinting with mass spectrometry to probe the structure of macromolecular complexes. Annu. Rev. Biophys. Biomol. Struct. *35*, 251–276.

Tien, A.H., and Sadar, M.D. (2018). Order within a disordered structure. Structure *26*, 4–6.

Tien, M.Z., Meyer, A.G., Sydykova, D.K., Spielman, S.J., and Wilke, C.O. (2013). Maximum allowed solvent accessibilities of residues in proteins. PLoS One *8*, e80635.

Tora, L., White, J., Brou, C., Tasset, D., Webster, N., Scheer, E., and Chambon, P. (1989). The human estrogen receptor has two independent nonacidic transcriptional activation functions. Cell *59*, 477–487.

Uversky, V.N. (2002). Natively unfolded proteins: a point where biology waits for physics. Protein Sci. *11*, 739–756.

Valentini, E., Kikhney, A.G., Previtali, G., Jeffries, C.M., and Svergun, D.I. (2015). SASBDB, a repository for biological small-angle scattering data. Nucleic Acids Res. *43*, D357–D363.

van der Lee, R., Buljan, M., Lang, B., Weatheritt, R.J., Daughdrill, G.W., Dunker, A.K., Fuxreiter, M., Gough, J., Gsponer, J., Jones, D.T., et al. (2014). Classification of intrinsically disordered regions and proteins. Chem. Rev. *114*, 6589–6631.

Vitalis, A., and Pappu, R.V. (2009). ABSINTH: a new continuum solvation model for simulations of polypeptides in aqueous solutions. J. Comput. Chem. *30*, 673–699.

Wang, L., and Chance, M.R. (2017). Protein footprinting comes of age: mass spectrometry for biophysical structure assessment. Mol. Cell Proteomics *16*, 706–716.

Wang, L., Friesner, R.A., and Berne, B.J. (2011). Replica exchange with solute scaling: a more efficient version of replica exchange with solute tempering (REST2). J. Phys. Chem. B *115*, 9431–9438.

Warnmark, A., Wikstrom, A., Wright, A.P.H., Gustafsson, J.A., and Hard, T. (2001). The N-terminal regions of estrogen receptor alpha and beta are unstructured in vitro and show different TBP binding properties. J. Biol. Chem. *276*, 45939–45944.

Wilkins, M.R., Gasteiger, E., Bairoch, A., Sanchez, J.C., Williams, K.L., Appel, R.D., and Hochstrasser, D.F. (1999). Protein identification and analysis tools in the ExPASy server. Methods Mol. Biol. *112*, 531–552.

Wright, P.E., and Dyson, H.J. (2015). Intrinsically disordered proteins in cellular signalling and regulation. Nat. Rev. Mol. Cell Biol. *16*, 18–29.

Yang, S., Blachowicz, L., Makowski, L., and Roux, B. (2010). Multidomain assembled states of Hck tyrosine kinase in solution. Proc. Natl. Acad. Sci. U S A *107*, 15757–15762.

Zhang, W., and Chen, J. (2014). Replica exchange with guided annealing for accelerated sampling of disordered protein conformations. J. Comput. Chem. *35*, 1682–1689.

Zheng, W., Borgia, A., Buholzer, K., Grishaev, A., Schuler, B., and Best, R.B. (2016). Probing the action of chemical denaturant on an intrinsically disordered protein by simulation and experiment. J. Am. Chem. Soc. *138*, 11702–11713.

STAR★METHODS

KEY RESOURCES TABLE

REAGENT or RESOURCE	SOURCE	IDENTIFIER
Bacterial and Virus Strains		
BL21(DE3)	NEB	Cat#C2527I
DH5-alpha	NEB	Cat#C2987H
pMCSG7	DNASU Plasmid depository	Vector id 367
Rosetta (DE3) pLysS	EMD Millipore	Cat#709563
Chemicals, Peptides, and Recombinant Proteins		
protease inhibitor cocktail	Roche	Cat#04693132001
Deuterium oxide	Millipore	Cat#S5733466
BTFA (3-Bromo-1,1,1-trifluoroacetone)	Alfa Aesar	Cat#A14948
Critical Commercial Assays		
Talon resin	Clontech	Cat#635503
Ni resin	Thermo	Cat#88222
agarose immobilized pepsin	Thermo Scientific	Cat#20343
Lys-C	Promega	Cat#VA1170
Asp-N	Promega	Cat#VA1160
Oligonucleotides		
S118D-FWD:5'-CGCCGCAGCTGGACCCTTTCCTGCAG-3'	Invitrogen	N/A
S118D-REV:5'-CTGCAGGAAAGGGTCCAGCTGCGGCG-3'	Invitrogen	N/A
S118C FWD:5'-CCGCCGCAGCTGTGCCCTTTCCTGCAGC-3'	Invitrogen	N/A
S118C REV:5'-GCTGCAGGAAAGGGCACAGCTGCGGCGG-3'	Invitrogen	N/A
L31A FWD:5'-tgaaccgtccgcaggccaagatccccctgg-3'	Invitrogen	N/A
L31A REV:5'-ccaggggggatcttggcctgcggacggttca-3'	Invitrogen	N/A
K32A,I33A,P34A FWD: 5'-aaccgtccgcagctcgcggccgccctggagcggcccc-3'	Invitrogen	N/A
K32A,I33A,P34A REV: 5'-ggggccgctccagggcggccgcgagctgcggacggtt-3'	Invitrogen	N/A
Experimental Models: Organisms/Strains		
Homo sapiens ESR1	This paper	UniProt: P03372 (1-184)
Software and Algorithms		
MestReNova	Mestrelab Research	http://mestrelab.com/software/mnova-suite
Topspin 3.2	Bruker, Inc	https://www.bruker.com/service/support-upgrades/software-downloads/nmr/free-topspin-processing/free-topspin-download.html
CRYSOL	(Svergun et al., 1995)	https://www.embl-hamburg.de/biosaxs/crysol.html
Fast-SAXS-pro	(Ravikumar et al., 2013)	http://www.theyanglab.org/saxs.html
iSPOT	(Huang et al., 2016)	http://www.theyanglab.org/ispot
PF-FP	(Huang et al., 2015)	http://www.theyanglab.org/protection.html
Deposited Data		
SAXS for NTD	This paper	SASBDB: SASDEE2
Structural models (NIAUF)2	This paper	PDB-dev: PDBDEV_00000027
MS data	This paper	PRIDE: PXD011361

CONTACT FOR REAGENT AND RESOURCE SHARING

Further information and requests for reagents may be directed to and will be fulfilled by the Lead Contact Sichun Yang (sichun.yang@case.edu).

METHOD DETAILS

Plasmid Construct

The sequence of the N-terminal domain (NTD) of human ERα (M1-Y184) was inserted into a bacterial expression vector pMCSG7 containing an N-terminal 6-Histidine tag designed for Ni-NTA affinity purification. Verification of this expression vector was performed for DNA sequencing. His-tag was cleaved by TEV protease to generate the NTD protein with a short three-residue segment of SNA (from the expression vector) at its N-terminus.

Protein Expression and Purification

The NTD samples were expressed as inclusion bodies in bacterial BL21 (DE3) cells. Expression was carried out overnight at 18°C with 0.1 mM IPTG in TB medium after the OD_{600} reached ∼0.8. Cells were harvested by centrifugation at 5000 rpm, re-suspended in 50 mM Tris, pH 8.0, 500 mM NaCl with a protease inhibitor cocktail (Roche, Indianapolis, IN). The cells were disrupted using a M110Y microfluidizer (Microfluidics, Newton, MA). The pellet fraction containing the NTD inclusion bodies was solubilized in the buffer of 50 mM sodium phosphate, pH 7.4, 300 mM NaCl, 6 M guanidine hydrochloride, and 5 mM imidazole with 1 mM PMSF. Solubilized inclusion bodies were centrifuged at 18,000×g for 45 min at 4°C. Cleared supernatant was incubated with Talon resin (Clontech) for 45 min at 4°C, followed by a wash with a buffer of 50 mM sodium phosphate, pH 7.4, 500 mM NaCl, 5 mM imidazole, and 6 M guanidine hydrochloride. Samples were step-eluted with imidazole at a series of concentrations of 50, 250, and 500 mM. Fractions containing the His-tagged NTD protein were combined and dialyzed against a buffer of 20 mM Tris, pH 7.5, 10 mM NaCl and 0.1 mM PMSF. Refolded NTD proteins were collected and incubated with TEV protease at a TEV:NTD ratio of 1:50 overnight at 4°C. The second step of affinity purification via Talon resin was used to remove the TEV and uncleaved His-tagged proteins. Final purification was performed using ion exchange via a HiTrap Q 5 mL column (GE Healthcare) and by gel filtration via an Enrich SEC650 column (Bio-Rad).

Circular Dichroism Spectroscopy

NTD proteins in a buffer of 20 mM sodium phosphate (pH 7.4) were used for the far UV CD spectroscopy measurement at 25°C on an AVIV 215 spectrometer with a 0.1 cm quartz cell. CD spectra were recorded in the wavelength of 190-260 nm. Each CD spectra were reported after buffer subtraction. Final spectra were averaged over three independent scans.

Two-Dimensional NMR Spectroscopy

Two-dimensional NMR spectra were recorded at 8°C on a Bruker Avance II 800-MHz spectrometer equipped with a TXI cryoprobe. The NTD protein was prepared in the buffer of 10 mM sodium phosphate, pH 7.2, 100 mM NaCl, 0.5 mM EDTA and 0.1mM PMSF, in the presence of 0 M, 3 M, 6 M urea, respectively, with a final protein concentration of 100 μM. Here, urea was used to replace GdnHCl because of its chemical compatibility for NMR spectroscopy. Two-dimensional ^{1}H-^{15}N TROSY spectra were collected with 1024*248 (F1*F2) points and 64 scans. In addition, one-dimensional proton spectra were recorded, where the ^{1}H chemical shifts of Arginine side chains (at 6.92 ppm and 6.97 ppm) were identified and used as a reference to calibrate the ^{1}H-^{15}N TROSY spectra. Spectra were processed with NMRPipe (Delaglio et al., 1995) and analyzed with Sparky (Goddard TD, Kneller DG, SPARKY 3, University of California, San Francisco).

Small-Angle X-Ray Scattering

A flow-cell setup was used for SAXS measurements at the LiX-16-ID beamline at the National Synchrotron Light Source II of the Brookhaven National Laboratory (Upton, NY). A series of scattering images were recorded each with a 2-sec exposure for both protein and buffer samples. Final scattering intensity was reported after buffer subtraction. The X-ray energy was 13 KeV.

Amide Hydrogen Exchange with Mass Spectrometry

Purified NTD (4.6 ug/ul) was prepared in 20 mM sodium phosphate buffer (pH 7.4). To initiate the deuterium labeling, 1ul aliquots of purified NTD were added to 19 μl of 10 mM phosphate buffer (pH 7.3) in D_2O. After incubation at room temperature for different time periods (1 min and 5 min), samples were cooled on ice in a pre-calibrated quenching 0.1 M phosphate buffer (pH 2.4) containing 7 M GdnHCl and 0.1 M TCEP. The solution was diluted 10 times with ice-cold 0.05% trifluoroacetic acid and digested for 5 min with agarose immobilized pepsin (Thermo Scientific). Peptic fragments were separated and analyzed by an LTQ Orbitrap XL mass spectrometer (ThermoElectron, San Jose, CA) as described previously (Smirnovas et al., 2009, 2011). As a result, the percent deuterium uptakes were averaged for the triplicate samples of NTD under each condition to obtain the mean percent deuterium incorporation.

Hydroxyl Radical Protein Footprinting and Protection Factor Analysis

NTD samples were purified into a buffer of 10 mM sodium phosphate, 0.05mM EDTA and pH 7.4. The protein concentration was adjusted to 5 μM. Samples were exposed to X-ray white beam for 0-50 ms at the 3.2.1 beamline of Advanced Light Source (Berkeley, CA) at ambient temperature, and immediately quenched with 10 mM methionine amide to prevent secondary oxidation. Subsequently, all samples were reduced with 10 mM DTT at 56°C for 45 minutes and alkylated with 25 mM iodoacetamide at room temperature in the dark for 45 minutes. Two sets of protease digestion were performed at 37°C using an enzyme-to-protein ratio of 1:10 (w/w). One was with Lys-C (Promega, Inc.) overnight, followed by Asp-N (Promega, Inc.) for 5 hours. The other was with

pepsin (Promega, Inc.) for 2 hours. Digestion was terminated by heating samples at 95°C for 2 min. Identification and quantification of oxidative sites were performed by liquid chromatography-mass spectrometry (LC-MS) analysis using an Orbitrap Elite mass spectrometer (Thermo Scientific, CA) interfaced with a Waters nanoAcquity UPLC system (Waters, MA). The proteolytic peptides (150 ng) were loaded on a trap column (180 μm × 20 mm packed with C18 Symmetry, 5 μm, 100 Å; Waters, MA) to desalt and concentrate peptides. Peptide mixture was eluted on a reverse phase column (75 μm x 250 mm column packed with C18 BEH130, 1.7 μm, 130 Å; Waters, MA) using a gradient of 2 to 35% mobile phase B (0.1% formic acid and acetonitrile) vs. mobile phase A (100% water/0.1 % formic acid) for 60 minutes at 40°C at a flow rate of 300 nL/min. Eluted peptides were introduced into the nano-electrospray source at a capillary voltage of 2.5 kV.

The extent of oxidation by MS was quantified as a function of X-ray exposure time. The curves were fit to an exponential decay function and the measured rate constants (k_{fp}) were divided by a measure of their intrinsic reactivity with hydroxyl radicals (k_R), thereby providing a residue-level protection factor (PF=k_R/k_{fp}) (Huang et al., 2015; Kaur et al., 2015). The PF calculation is available from the website http://www.theyanglab.org/protection.html. The log of the PF values provides an accurate surface topology map, where high logPF values reflect more protection for solvent and lower logPF values reflect greater solvent exposure.

Conformational Library

A pool of 35,240 NTD structure candidates was generated from molecular dynamics simulations with an accumulative total time of 35-μs in a 1-ns recording frequency. To enhance conformational sampling, two advanced algorithms were used: Gaussian accelerated molecular dynamics (GaMD) (Miao et al., 2015) and replica exchange solute tempering (REST2) (Wang et al., 2011). First, a set of 25 GaMD trajectories (using the software AMBER16, each starting with a random configuration and lasting 1 μs) resulted in a total of 25 μs. Second, a set of 64 replicas in REST2 simulations, ranging from 300 K to 600 K were performed at the Argonne Leadership Computing Facility using the software NAMD as previously described (Jo and Jiang, 2015; Phillips et al., 2005). Each replica lasted 160 ns, which resulted in 10 μs. In both GaMD and REST2 simulations, the molecular force field of Amber ff99SB with a TIP3P water model was used (Hornak et al., 2006). Given that the force field for IDPs is still under active development (Best et al., 2014; Huang and MacKerell, 2018; Huang et al., 2017; Nerenberg and Head-Gordon, 2018; Piana et al., 2015; Song et al., 2017), the Amber ff99SB was used here for the purpose of pose generation only, with the help from the inclusion of all trajectories from different temperatures and nonequilibrium simulations. Hence, the accuracy of the force field used is beyond the scope here, and these conformations were combined and selected by comparison with multi-technique experimental measurements. To group similar structures together and reduce the computational cost, we performed an RMSD-based clustering analysis as previously described (Huang et al., 2016; Svergun, 1992). Using a Ca-RMSD cutoff of 5 Å, we obtained a set of N=8,491 clusters of NTD structures from the total of 35,240 simulation snapshots.

Ensemble Structure Construction

Based on the library of NTD conformations generated above, data from SAXS and FP-PF measurements were combined for ensemble refinement. We selected the ensemble-structures that best-fit experimental SAXS and FP-PF data simultaneously, by a weighted average over the resulting N clusters of structures with a probability distribution $\{P_i\} = P_1, \cdots, P_N$ of each cluster (i), based on two unit-less functions χ^2 and φ^2. The χ^2 is defined to measure the difference between the theoretical and experimental SAXS profile by (Yang et al., 2010),

$$\chi^2(\{P_i\}) = \frac{1}{N_q} \sum_q \frac{\left\{ \log I^{exp}(q) - \sum_{i=1}^N \log\left[P_i \cdot I_i^{cal}(q)\right] \right\}^2}{\sigma^2(q)},$$ (Equation 1)

where I^{cal} is calculated using fast-SAXS-pro (Ravikumar et al., 2013) and N_q is the number of scattering q points recorded in experimental I^{exp} (with its measurement error of $\sigma(q)$). Similarly, the φ^2 is the goodness of fit between experimental and theoretical FP-FP data by (Hsieh et al., 2017; Huang et al., 2016, 2018),

$$\varphi^2(\{P_i\}) = \frac{1}{N_s} \sum_s \frac{\log PF^{exp}(s) - \sum_{i=1}^N \log\left[P_i \cdot SA_i^{cal}(s)\right]^2}{\delta^2(s)},$$ (Equation 2)

where SA^{cal} is the predicted side-chain SA value of each site, using the linear regression between experimental $\log PF^{exp}$ values (with an error $\delta(s)$ at each site (s)) and SA values of N_s sites for each structural cluster (here, N_s=16 as shown in Table S3).

To avoid potential overfitting, we performed a maximum-likelihood principle analysis by adopting a "relative entropy" contribution (Boomsma et al., 2014; Rozycki et al., 2011),

$$S = -\sum_{i=1}^N P_i \log P_i,$$ (Equation 3)

assuming a uniform prior, so the entire optimization of the probability distribution was achieved by minimizing an effective free energy,

$$F(\{P_i\}) = \chi^2 + \beta\varphi^2 - TS,$$ (Equation 4)

where β is a scaling factor for balancing two unit-less functions χ^2 and φ^2 and T is an effective temperature-like scaling factor. We chose $\beta = 0.1$ and $T = 0.05$ by minimizing $F(\beta,T)$ (see Figure S3). To reduce the computational cost, we decreased the number of clusters to N=519 by satisfying a cutoff criteria of $\chi^2 < 5$ and a negative linear correlation between logPF and SA for each cluster. Finally, an optimal probability distribution $\{P_i\}$ was determined by numerically minimizing Equation 4 with the constraints of $0 < P_i < 1$ and $\sum_i P_i = 1$ using a genetic algorithm (Conn et al., 1997).

Ensemble Contact Map

The residue-residue interaction (or contact) was calculated using the *contact of structural units* (CSU) approach (Sobolev et al., 1999). Each residue was the center of a window segment of 5 neighboring amino acids. Each contact was weighted over the ensemble-structures by the probability of top 100 structures that account for a total of 80% of the entire population.

Surface Plasmon Resonance

The binding of NTD with TBP was measured in PBSP+ (GE healthcare) buffer, pH7.4 by surface plasmon resonance (SPR) using a Biacore T100 system (GE Healthcare) at 4°C. S series sensor chip CM4 (GE Healthcare) was preconditioned at 100uL/min with successive 20 μL pulses of 50 mM NaOH, 100 mM HCl, 0.1 mM SDS and 0.085% (v/v) H_3PO_4. NTD was immobilized at low density and TBP concentration series ranging from 1.5 to 25 μM were injected over the NTD surface. Data were plotted by Origin 2017 and the affinity constant was calculated by Biaevaluation3 software (GE Healthcare).

Fluorine-19 NMR Spectroscopy

The NTD^{S118C}-BTFA protein was prepared by site-directed mutation of S118C and BTFA (3-Bromo-1,1,1-trifluoroacetone, Alfa Aesar Cat# A14948) was added during the solubilization of inclusion bodies with a 1000-fold dilution and further incubated overnight at 4°C. The final NTD-BTFA protein was exchanged into a buffer of 10mM sodium phosphate, pH 7.2, 0.5 mM EDTA, and 0.1 mM PMSF. The final protein concentration used for ^{19}F-NMR is 2.0 mg/ml, 1.6 mg./ml, and 2.1 mg/ml for the wild-type, L31A, the triple mutant K32A/I33A/P34A of the NTD^{S118C}-BTFA, respectively. A volume of 250 μl was used for each protein sample containing 10% D_2O as an initial point for D_2O titration from 10% to 50%.

One-dimensional ^{19}F-NMR experiments were performed on a 500 MHz Bruker Ascend III HD spectrometer equipped with a nitrogen-cooled ^{19}F tuned BBO probe. Spectra were acquired with 512 scans, 131K data points in the direct dimension, a pulse length of 15.0 μsec, a spectral width 468750 Hz (^{19}F), a digital resolution of 3.5 Hz/point, and a relaxation delay of 1.0 s at the temperature of 281 K. The data was processed with Topspin 3.2 software and free induction decay (FID) signals were apodized with an exponential window function as to line broadening of 0.30 Hz.

QUANTIFICATION AND STATISTICAL ANALYSIS

Duplicates were performed for protein footprinting and standard deviations were indicated. SAXS data uncertainties were derived from a total of five scattering images. The ensemble fitting calculations were repeated nine times; reported probability values are the average and standard deviation for the replicated calculations.

DATA AND SOFTWARE AVAILABILITY

The SAXS data and three representative structures for the NTD ensemble derived from in-house multi-technique modeling have been deposited in the Small Angle Scattering Biological Databank (SASBDB: SASDEE2; https://www.sasbdb.org/data/SASDEE2). A set of 10 integrative ensemble-structures of the ERα-NRD have been deposited to the multi-scale I/H structure PDB-dev database (PDB-dev: PDBDEV_00000027; https://pdb-dev.wwpdb.org/static/cif/PDBDEV_00000027.cif). Footprinting-related mass spectrometry (MS) data (raw and search files) have been deposited into the ProteomeXchange Consortium (PRIDE: PXD011361; https://doi.org/10.6019/PXD011361). Other data are available from the corresponding author upon reasonable request.

Supplemental Information

A Metastable Contact and Structural Disorder

in the Estrogen Receptor Transactivation Domain

Yi Peng, Shufen Cao, Janna Kiselar, Xiangzhu Xiao, Zhanwen Du, An Hsieh, Soobin Ko, Yinghua Chen, Prashansa Agrawal, Wenwei Zheng, Wuxian Shi, Wei Jiang, Lin Yang, Mark R. Chance, Witold K. Surewicz, Matthias Buck, and Sichun Yang
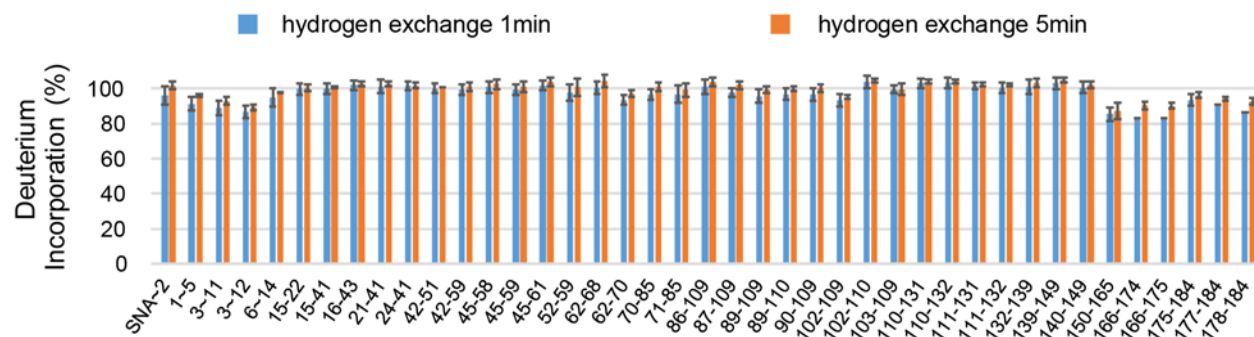
Figure S1. Related to Figure 1. Deuterium incorporation of peptic fragments in HX-MS within 1 min (blue) and 5 min (red) incubation in D_2O. Error bars indicate standard deviation (three independent experiments).
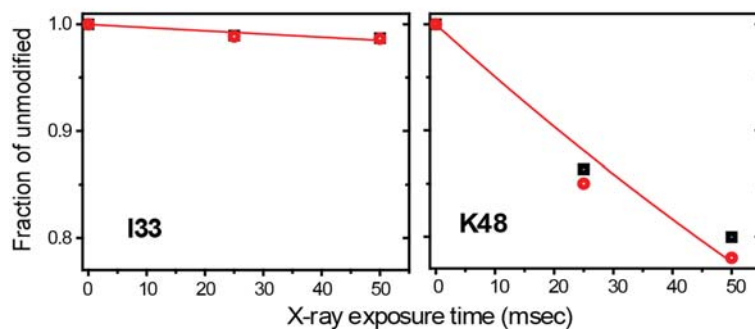
Figure S2. Related to Figure 4. Hydroxyl radical protein footprinting dose-response curves as a function of X-ray exposure time. Red lines are the least-squares fit to an exponential decay function (i.e., a normalized fraction of unmodified residues), each yielding a rate of footprinting (k_{fp}). The division by an intrinsic reactivity with hydroxyl radicals (k_R) provides a protection factor measure (PF = k_R/k_{fp}).
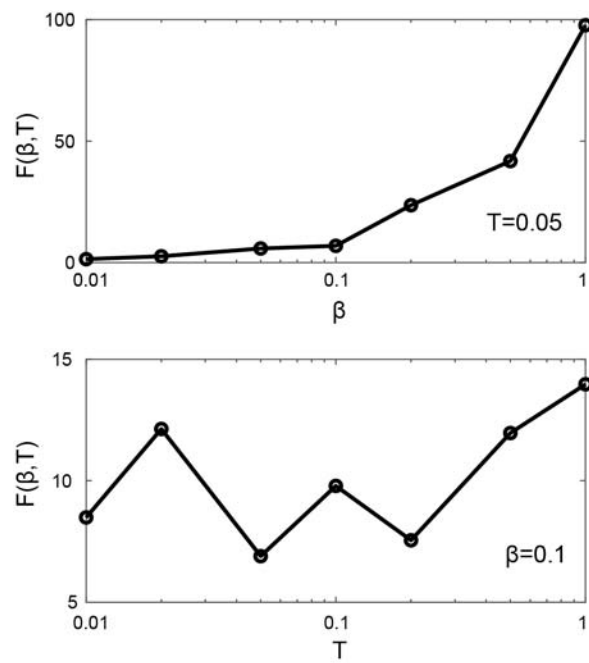
Figure S3. Related to Figure 4. The effective free energy F(β,T) as function of the parameters β

and T. The values of β=0.1 and T=0.05 were chosen to give the local minimum of F(β,T) (see
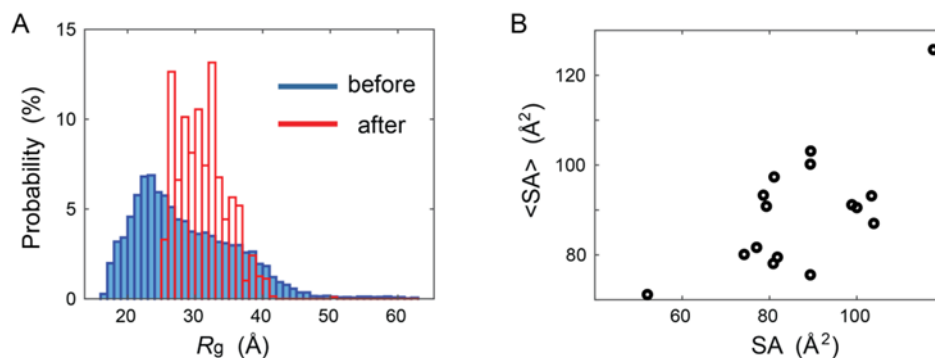
Eq. 4).

Figure S4. Related to Figure 4. Structure selection by the ensemble-fitting method against experimental scattering and footprinting data. (A) The histogram plot as a function of R_g before and after the ensemble fitting was applied. (B) The ensemble-averages of solvent-accessible surface area for the set of 16 footprinting-probed residues before (<SA>) and after (SA) the ensemble-fitting.
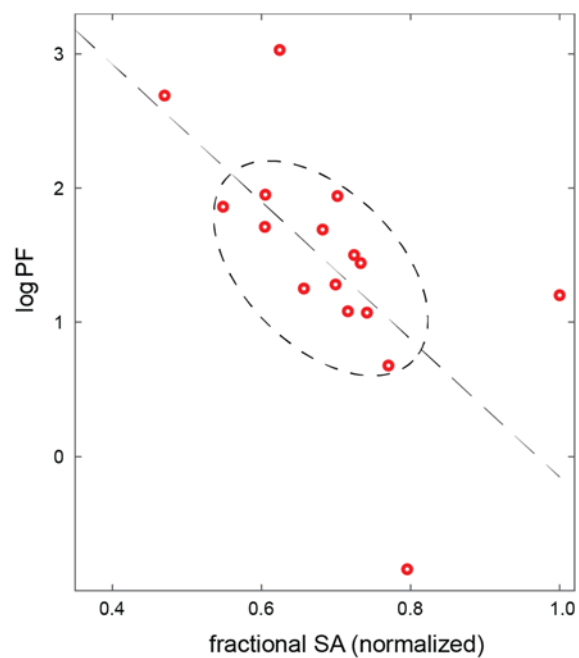
Figure S5. Related to Figure 4. Measured logPF values against the fractional SA values for the set of 16 probed residues. The factional SA value was the SA weighted by each residue's maximum possible accessible area.
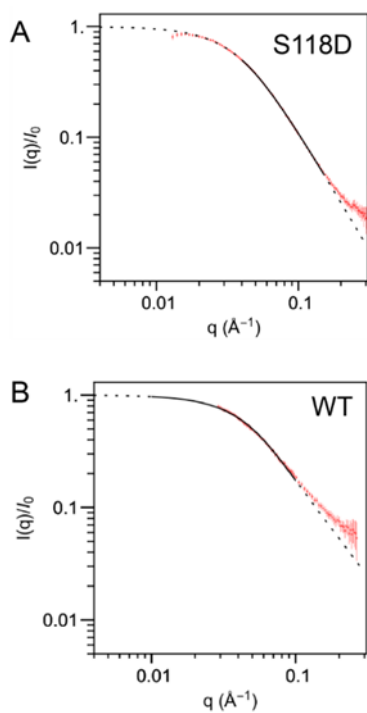
Figure S6. Related to Figure 5. SAXS data for mutant S118D (A), compared to the wild-type
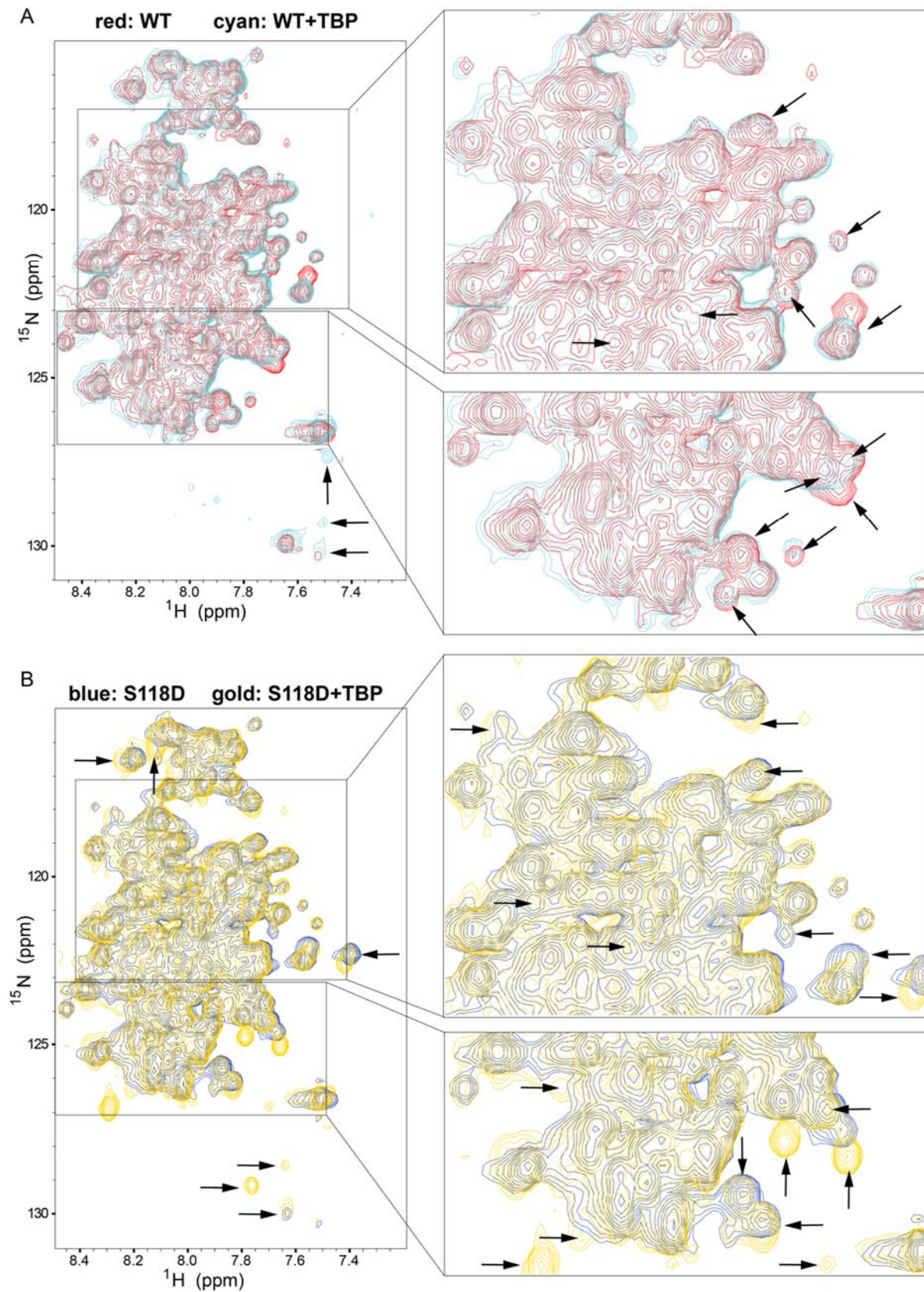
(B). Generated using the webserver at http://sosnick.uchicago.edu/SAXSonIDPs.

Figure S7. Related to Figure 5. Mutation-induced conformational changes and alteration of

coactivator TBP binding.

(A) Overlap of ^{1}H-^{15}N TROSY spectra of the WT in the absence (red) and presence (cyan) of TBP. Change/shift of peaks is marked by arrows.

(B) Overlap of ^{1}H-^{15}N TROSY spectra of S118D in the absence (blue) and presence (gold) of TBP.

Table S1. Related to Figure 4. SAXS data details and parameters.

Experiment date	June 12, 2017
SASBDB ID (https://www.sasbdb.org)	SASDEE2 (https://www.sasbdb.org/data/SASDEE2)
Beamline/Instrument	NSLS-II/16-ID-LiX, Pitaus3 S 1M/300k
Wavelength	0.9 Å
Sample detector distance	4.270 m / 0.856 m
Exposure time	1 second
Cell temperature	10 °C
protein concentration	2.5 mg/ml
Number of residues	187
Molecular weight	20.18 kDa
Protein buffer	20mM Hepes, pH7.4, 300mM NaCl, 5% glycerol, 1mM DTT, 0.5 mM PMSF, 1 mM EDTA

Table S2. Related to Figure 4. Radius of gyration (R_g) values derived from SAXS data using several fitting methods.

WT/S118D	Guinier	Debye	extended Guinier	Sosnick
R_g (Å)	30.0±1.6/35.8±0.5	32.9± 0.6/41.0±0.3	29.2±1.3/36.7±0.6	31.0±0.2/38.7±0.2
$(qR_g)_{max}$	1.3	3.0	2.0	3.0/5.2
reference	(Guinier, 1939)	(Debye, 1947;Calmettes et al., 1994)	(Zheng and Best, 2018)	(Riback et al., 2017)

Table S3. Related to Figure 4. Hydroxyl radical protein footprinting protection factors (FP-PFs) for the NTD residues. Listed are the probed residues and their corresponding values for footprinting rates (k_{fp}), logPF, and SA^{pred} predicted from the ensemble-structures.

Residue	k_{fp} (s^{-1})	log(PF)	SA^{pred} (Å^2)
L26	0.63±0.01	1.94±0.02	79.3
L31	1.26±0.14	1.25±0.11	74.2
I33	0.30±0.03	2.69±0.10	52.0
L35	1.50±0.13	1.08±0.09	80.9
L39	0.81±0.04	1.69±0.05	77.0
L44	0.98±0.20	1.50±0.20	81.8
K48	5.07±0.30	-0.84±0.06	117.6
Y54	1.70±0.15	1.95±0.09	89.4
Y73	2.17±0.09	1.71±0.04	89.3
Y80	1.87±0.092	1.86±0.05	81.0
F89	3.85±0.11	1.07±0.03	100.0
F97	5.68±0.19	0.68±0.03	103.9
F120	2.64±0.11	1.44±0.04	98.9
H124	0.45±0.029	3.03±0.07	78.6
Y130	3.32±0.13	1.28±0.04	103.4
P146	0.30±0.02	1.20±0.07	89.3